Naval Surface Warfare Center
Carderock Division
West Bethesda, MD 20817-5700

NSWCCD-61-TR-2020/18 **August 2020**

Platform Integrity Department

Technical Report

Validation of Materials-Informed Digital Twin: Mapping Residual Strains in HSLA Steel Weldment using High Energy X-rays

by

Charles R. Fisher

Kelly E. Nygren

Armand J. Beaudoin

Validation of Materials-Informed Digital Twin: Mapping Residual Strains in HSLA Steel Weldment using High Energy X-rays

NSWCCD-61-TR–2020/18

Naval Surface Warfare Center
Carderock Division
West Bethesda, MD 20817-5700

NSWCCD-61-TR-2020/18 **August 2020**

Platform Integrity Department
Technical Report

Validation of Materials-Informed Digital Twin: Mapping Residual Strains in HSLA Steel Weldment using High Energy X-rays

by

Charles R. Fisher
Kelly E. Nygren
Armand J. Beaudoin

REPORT DOCUMENTATION PAGE

Form Approved
OMB No. 0704-0188

1. REPORT DATE *(DD-MM-YYYY)* 13-08-2020	**2. REPORT TYPE** Technical Report	**3. DATES COVERED** *(From - To)* FEB 2019 - NOV 2019

4. TITLE AND SUBTITLE

Validation of Materials-Informed Digital Twin: Mapping Residual Strains in HSLA Steel Weldment using High Energy X-rays

5a. CONTRACT NUMBER N/A

5b. GRANT NUMBER N/A

5c. PROGRAM ELEMENT NUMBER N/A

6. AUTHOR(S)

Charles R. Fisher
Kelly E. Nygren
Armand J. Beaudoin

5d. PROJECT NUMBER N/A

5e. TASK NUMBER N/A

5f. WORK UNIT NUMBER N/A

7. PERFORMING ORGANIZATION NAME(S) AND ADDRESS(ES) AND ADDRESS(ES)

Naval Surface Warfare Center,
Carderock Division, Code 611
9500 MacArthur Boulevard
West Bethesda, MD 20817-5700

Cornell High Energy Synchrotron
Source (CHESS)
161 Synchrotron Drive
Ithaca, NY 14853

8. PERFORMING ORGANIZATION REPORT NUMBER

NSWCCD-61-TR-2020/18

9. SPONSORING / MONITORING AGENCY NAME(S) AND ADDRESS(ES)

Krista Michalis
Program Manager, NISE 219
Naval Surface Warfare Center,
Carderock Division

10. SPONSOR/MONITOR'S ACRONYM(S)

11. SPONSOR/MONITOR'S REPORT NUMBER(S)
N/A

12. DISTRIBUTION / AVAILABILITY STATEMENT

DISTRIBUTION A. Approved for public release: distribution unlimited.

13. SUPPLEMENTARY NOTES

14. ABSTRACT:

The U.S. Navy has placed an emphasis on establishing digital twin prototypes across all of its assets. However, material processing data is not currently included in simulations for structural performance, which could lead to inaccuracies in lifecycle analysis. Integrated Computational Materials Engineering (ICME) techniques yield a path to solving this problem through linking digital information across multiple length scales in order to minimize the time and cost of physical testing needed for validation.

This report is part of a planned four-part series detailing the entire materials-informed digital twin effort. This report details the selection and fabrication of the "sister sample" specimens, finite-element analysis (FEA)-based welding simulations of the final reinforced dog-bone weldment, and comparison of predicted strain data to two-dimensional (2D) strain maps produced at the Cornell High-Energy Synchrotron Source (CHESS). The second report will detail additional FEA analysis of rolled plate in comparison to through-thickness strain measurement at CHESS. The third report will detail efforts to further validate the CHESS measurements at neutron diffraction facilities. Lastly, the fourth report will include FEA simulations of mechanical performance (with incorporated material processing data) in comparison to physical testing of the final weldment.

As part of the current effort, a set "sister-samples" to represent various steps in the fabrication process was produced from a single plate of 25.4 mm (1-in.) thick HSLA-100 steel. Specimen #1 represented incoming rolled plate, Specimen #2 represented cut pieces, and Specimen #3 represented the final reinforced dog-bone welded structure. Initial FEA analysis of the final weldment showed high tensile stresses near the weld passes in the heat-affected zone (HAZ), as expected. Validation of the predicted strain within the dog-bone shape was completed using EDD measurements at CHESS. The results showed high correlation between the measured EDD data and the FEA predictions, particularly for the high strain (>0.0015) fields of first principle strain vectors measured parallel to each welding pass. The computational validation is the first step towards validating the materials-informed digital twin method for increasing accuracy of structural analysis and fatigue lifecycle evaluation.

15. SUBJECT TERMS

ICME, CWM, SYSWELD, Computational Simulation, Steel, Welding, X-Ray, EDD, Strain, Residual Stress

16. SECURITY CLASSIFICATION OF: UNCLASSIFIED			**17. LIMITATION OF ABSTRACT**	**18. NUMBER OF PAGES**	**19a. RESPONSIBLE PERSON** Charles Fisher
a. REPORT UNCLASSIFIED	**b. ABSTRACT** UNCLASSIFIED	**c. THIS PAGE** UNCLASSIFIED		37	**19b. TELEPHONE NUMBER** (301) 227-4969

CONTENTS

FIGURES

TABLES

ADMINISTRATIVE INFORMATION

The work described in this report was performed by the Welding, Processing, and Nondestructive Evaluation Branch (Code 611) of the Platform Integrity Department at the Naval Surface Warfare Center, Carderock Division (NSWCCD) and at the Cornell High Energy Synchrotron Source (CHESS) on the Materials Solution Network at CHESS (MSN-C) beamline. The NSWCCD work was funded in FY19 through the Naval Innovative Science and Engineering (NISE) Research and Development program at NSWCCD, as part of the project entitled *Integrated Computational Materials Engineering (ICME) Design and Simulation Tool Enhancement*. The work at CHESS was supported by the Air Force Research Laboratory (AFRL) under award FA8650-19-2-5220.

ACKNOWLEDGEMENTS

The authors would like to thank Carrie Davis, Jimmy Hayden, and Dan Root (NSWCCD Code 611); Richard Gins and Shawn Robinson (NSWCCD Code 612); and Arthur Woll, Matt Miller, Darren Pagan, Peter Ko, and Chris Budrow (CHESS) for their technical assistance in the completion of this work.

This page intentionally left blank

EXECUTIVE SUMMARY

The U.S. Navy has placed an emphasis on establishing digital twin prototypes across all of its assets. However, material processing data is not currently included in simulations for structural performance, which could lead to inaccuracies in lifecycle analysis. Integrated Computational Materials Engineering (ICME) techniques yield a path to solving this problem through linking digital information across multiple length scales in order to minimize the time and cost of physical testing needed for validation.

This report is part of a planned four-part series detailing the entire materials-informed digital twin effort. This report details the selection and fabrication of the "sister sample" specimens, finite-element analysis (FEA)-based welding simulations of the final reinforced dog-bone weldment, and comparison of predicted strain data to two-dimensional (2D) strain maps produced at the Cornell High-Energy Synchrotron Source (CHESS). The second report will detail additional FEA analysis of rolled plate in comparison to through-thickness strain measurement at CHESS. The third report will detail efforts to further validate the CHESS measurements at neutron diffraction facilities. Lastly, the fourth report will include FEA simulations of mechanical performance (with incorporated material processing data) in comparison to physical testing of the final weldment.

As part of the current effort, a set "sister-samples" to represent various steps in the fabrication process was produced from a single plate of 25.4 mm (1-in.) thick HSLA-100 steel. Specimen #1 represented incoming rolled plate, Specimen #2 represented cut pieces, and Specimen #3 represented the final reinforced dog-bone welded structure. Initial FEA analysis of the final weldment showed high tensile stresses near the weld passes in the heat-affected zone (HAZ), as expected. Validation of the predicted strain within the dog-bone shape was completed using EDD measurements at CHESS. The results showed high correlation between the measured EDD data and the FEA predictions, particularly for the high strain (>0.0015) fields of first principle strain vectors measured parallel to each welding pass. The computational validation is the first step towards validating the materials-informed digital twin method for increasing accuracy of structural analysis and fatigue lifecycle evaluation.

BACKGROUND

There is a desire to establish digital twin prototypes for assets across the entire U.S. Navy enterprise. These "digital twins" are a digital representation of a physical component, assembly, or product and will be used for lifecycle analysis and product management. However, material processing data, particularly residual stress distribution, is unable to be currently included for lifecycle analysis due to limitations with current computational toolsets. This represents a major hurdle to digital twin development, as residual stress induced from material processing and structural fabrication can cause severe degradation of structural performance [1]. Both Webster and Ezeilo [2] and Barsoum and Barsoum [3] found that proper structural fatigue life predictions require precise residual stress distribution knowledge. However, quantification of accumulated stress and its distribution throughout the shipbuilding process is not well characterized [4], especially for non-welding-related processing.

The Integrated Computational Materials Engineering (ICME) paradigm is "…the integration of materials information, captured in computational tools, within engineering product performance analysis and manufacturing-process simulation" [5]. ICME programs have evolved to solve major manufacturing issues, including: 1) decreasing material development time, 2) ensuring manufacturing competitiveness, and 3) increasing technological advantage. Specifically, ICME techniques have shown the potential to reduce the cost and time to design and deploy materials [6]. However, the strength of the ICME paradigm comes from linking digital information across multiple length scales in order to minimize the time and cost of physical testing, which has been a difficult undertaking.

Across the U.S. Navy, there are numerous groups working on extremely complex simulations ranging from structural design to material processing. However, due to the highly specialized nature of the technical expertise, the varied groups are not easily able to collaborate across digital tools. Therefore, to meet the materials-informed digital twin objective, a project was initiated to leverage ICME techniques in order to computationally link disparate software codes while validating the digital data with physical testing. This multi-year project links finite-element analysis (FEA) tools across plate processing, shape cutting and machining, welded fabrication, and structural performance. The FEA simulations were paired with physical measurement for verification and validation (V&V) of strain evolution in the final welded assembly. A digital comparison of the fatigue life for the part-level model both with and without fabrication information (i.e., residual stress from processing, machining, and welding) is essential to understanding how fabrication affects performance on larger prototypes and assets. Again, V&V techniques will be used to compare the simulation results with physical measurements. This novel simulation linkage across fabrication steps to mechanical performance will enable lifecycle and digital twin analysis for assets across the shipbuilding industry.

High-energy X-ray measurements were utilized to validate the simulation results and establish the digital thread between material processing FEA tools and structural FEA tools in order to inform how fabrication affects resultant lifecycle performance. The use of high-energy X-rays provided a powerful tool to measure not only surface strains, but also resolve strain gradients at depth across the various components investigated in the project. This was critical to verify the computational models across various fabrication steps as both machining and welding induces modification of through-thickness stresses. The following effort embraced experimental measurement with concomitant model validation: mapping of a subset of strain components provides validation of a weld process model. The expected state of residual stress does not follow from the measurement, but rather from the FEA model prediction. It was the spatial resolution of the experimental mapping that was key to validation. A prototype for the present effort was shown previously by Mach *et al.* [7]. Recent efforts have extended this general approach to a multiple-pass fillet weld model in comparison to neutron diffraction analysis and the contour method for V&V [8].

For HSLA-100, the material of concern with regard to the present effort, residual stress in quenched 60.75 mm (2.4-in.) thick HSLA-100 plate have been measured by the contour method by Prime [9]. The measurement was complemented by an FEA simulation to derive stress relaxation associated with sample removal from the parent plate. An expected pattern of an in-plane tensile component of stress balanced by compressive stresses on the top and bottom surfaces was found. The maximum values were roughly 200 MPa in the tension and compression regions. The relation of residual stress to texture and subsequent impact on residual stress determination in HSLA-100 was explored for variations in thermomechanical treatment by Bahadur *et al.* [10]. They also measured surface residual stress magnitudes around 200 MPa, but noted that the surface of the plate was in tension from the quenching process, highlighting the need to understand all steps in the fabrication process. Insight into weld thermal cycles of HSLA-100 was developed through characterization and simulation of microstructure combined with measurement of mechanical properties by Duch and Dupont [11].

This report is part of a planned four-part series detailing the entire material-informed digital twin effort. This report details the selection and fabrication of the specimens, welding simulations of the final component, and comparison of resultant data to two-dimensional (2D) strain maps produced at CHESS. The second report will detail additional FEA analysis of the rolled plate in comparison to through-thickness strain measurement at CHESS. The third report will detail efforts to validate the CHESS measurements at different neutron diffraction facilities. Lastly, the fourth report will include FEA simulations of mechanical performance (with integrated material processing data) in comparison to physical testing of the reinforced dog-bone weldment.

APPROACH

Specimen Fabrication

The selected plate used for all specimens within this project was nominally a 25.4 mm (1-in.) thick plate of high-strength low alloy (HSLA)-100 steel. The HSLA-100 plate conformed to the NAVSEA Technical Publication 300 Composition 1 specifications [12], which requires a minimum yield strength of 690 MPa (100 ksi). The chemical composition of the base material was confirmed at NSWCCD using glow discharge atomic emission spectrometry (GD-AES) on a Leco GDS900 in accordance with ASTM E415 [13] for all elements except carbon and sulfur; these elements were analyzed at NSWCCD on a Leco CS844 using a combustion technique in accordance with ASTM E1019 [14]. The mechanical properties of the plate were confirmed by testing at Westmoreland Mechanical Testing and Research, Inc. in Youngstown, PA using ASTM A370 [15].

Shape Cutting

The HSLA-100 plate had an original approximate width and length of 1.52 m by 4.27 m (5-ft by 14-ft). It was not a newly procured plate, but instead selected from previous stock to ensure weathering of the plate was included in the analysis, mimicking processes at a shipyard. In order to reduce the effect of the cutting process on the residual stress state of the plate, the water-jet cutting technique was selected for each cutting step. **Figure 1** shows images of the original plate plus the three sub-plates cut to a size of 61 cm by 30.5 cm (2-ft by 1-ft).

These sub-plates represented the three “sister samples” used throughout the materials-informed digital twin project. Instead of having a single specimen investigated at various points throughout the fabrication cycle, which would have increased the time requirements and cycle times for strain measurements at the various labs (CHESS, ORNL, and NIST), the sister samples were used to have each step in the fabrication process ready for a single session at each beamline. After the first cutting step to create the 61 cm by 30.5 cm (2-ft by 1-ft) sister samples, Specimen #1 was set aside for use as the “As-Received” condition having been through the plate rolling and heat treatment steps during plate fabrication.

Plate #2 and #3 were put through a second water-jet cutting step to create the dog-bone and arch shapes shown in **Figure 2**. Each specimen was cut to the same size requirements. The more detailed cutting diagrams for all three specimens are found in **Appendix A**. After the second round of cutting, Specimen #2 (both dog-bone and arch shape) was set aside for use as the “Post-Cutting” condition.

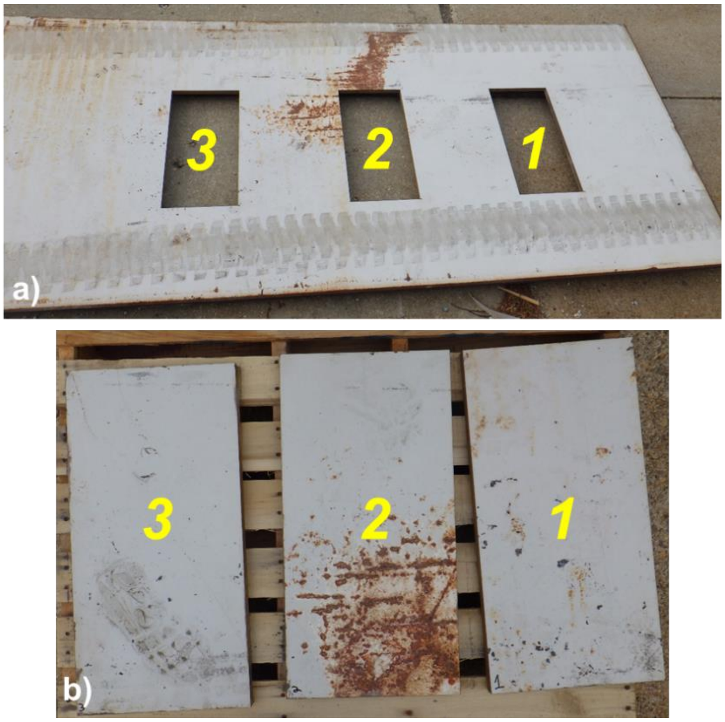

Figure 1. The 25.4 mm (1-in.) thick plate of HSLA-100 steel showing: **a)** the full 1.52 m by 4.27 m (5-ft by 14-ft) plate with the three 61 cm by 30.5 cm (2-ft by 1-ft) sub-plates removed, and **b)** the three sub-plates removed by water-jet cutting to serve as the "sister samples" for the project.

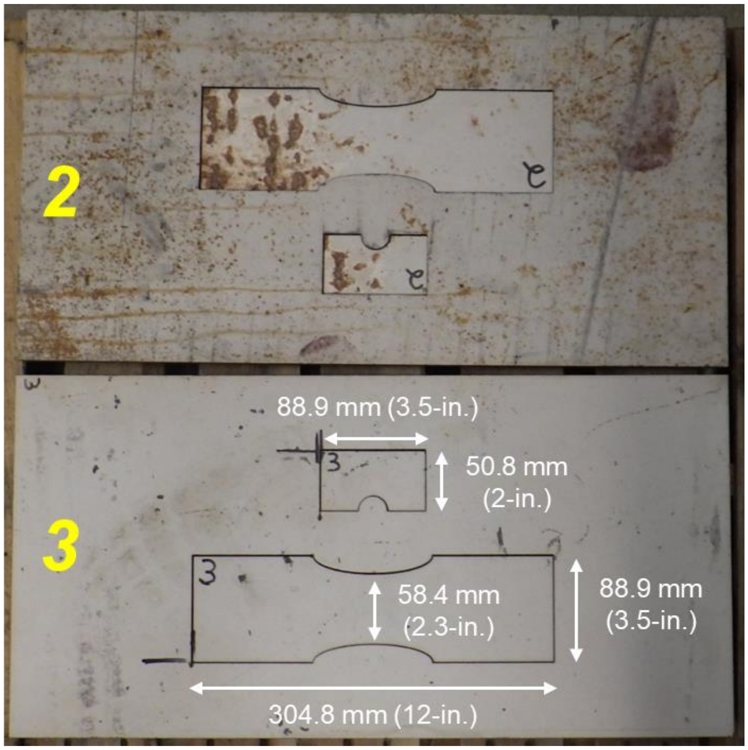

Figure 2. Plate #2 and #3 after the second water-jet cutting process to produce the dog-bone and arch shapes.

Welded Fabrication

The final fabrication step was welding the dog-bone and reinforcement arch shape together to create Specimen #3, shown in **Figure 3**. The final shape was determined by coordinating with the Performance Evaluation Branch (Code 653) to ensure the Specimen #3 could be fully tested mechanically at NSWCCD in a fatigue lifecycle scenario. In addition, the reinforcement arch welded in six locations (four longitudinally, two transverse) to the dog-bone shape increased the likelihood of high longitudinal and transverse strain gradients would be present post-welding.

Figure 3. Post-welding to produce the final component, Specimen #3.

The reinforcement arch was welded to the dog-bone shape using two different processes. First, a manual gas-tungsten arc welding (GTAW) process for the root passes on a Miller Dynasty 280 machine. Second, the fill and cover passes were completed with a manual gas-metal arc welding (GMAW) process on a Lincoln Electric PowerWave S500 machine. The filler metal used for both processes was ER100-s wire, with a diameter of 3.175 mm (0.125-in) for GTAW and 0.889 mm (0.035-in) for GMAW. The general parameters specified are shown below in **Table 1**. The measured parameters for each weld pass, as well as the weld sequencing used, are shown in **Appendix B**. Each longitudinal weld location consisted of a root GTAW pass, a filler GMAW pass, and two covering GMAW passes. Each transverse weld consisted of only a root GTAW pass and a covering GMAW pass. Pre-heating was completed with an oxyacetylene torch and no clamping was required. Each weld pass was completed with 1-2 minutes of the previous in order to meet the interpass temperature requirements. Room temperature was measured to be 20 °C (68 °F) with a relative humidity of 62%.

Table 1. Welding Parameters for Specimen #3 Fabrication

Parameter	GTAW	GMAW
Voltage (V)	7-9	24-26
Current (A)	25-45	170-190
Travel Speed (mm/s [ipm])	1.69-3.81 [4-9]	3.39-5.08 [8-12]
Heat Input (J/mm [kJ/in])	79-197 [2-5]	984-1299 [25-33]
Preheat Temperature	93-149 °C (200-300 °F)	
Interpass Temperature	93-149 °C (200-300 °F)	
Cover Gas	100% Ar	95% Ar, 5% O_2

Representative weld beads using similar parameters to those used for Specimen #3 were also prepared. The representative Tee-joint weld scenarios included: 1) GTAW root pass only, 2) GTAW root pass with single GMAW cover pass, and 3) GTAW root pass with three GMAW cover passes. Each representative joint was cross-sectioned, mounted, polished to a final grit of 0.04 µm using colloidal silica, and etched with fresh 2% Nital solution.

Computational Simulation

Specimen #3 was computational simulated using *SYSWELD*, a commercially-available welding-specific finite-element code from ESI. Simulations were set-up on the *Visual Weld* (version 14.5) module and run using the *SYSWELD* solver (version 2019.0). Solid elements and transient heat source simulation using a Goldak heat source model [16] were used analyze the distortion and stress evolution from the welding process. The V&V techniques utilized for the simulation are described in the American Welding Society (AWS) A9.5 *Guide for Verification and Validation in Computational Weld Mechanics* [17]. The cross-sections from the representative tee-joints ensured correct sizing for each weld pass. **Figure 4** shows an image of meshed FEA model, whereas **Figure 5** shows a cross-section of representative longitudinal and transverse weld joints showing the bead sizing. Note that the cross-sectional shapes were simplified to right triangles, as the physical weld joints did not show enough convex or concave shape to warrant mimicking the exact weld bead shape.

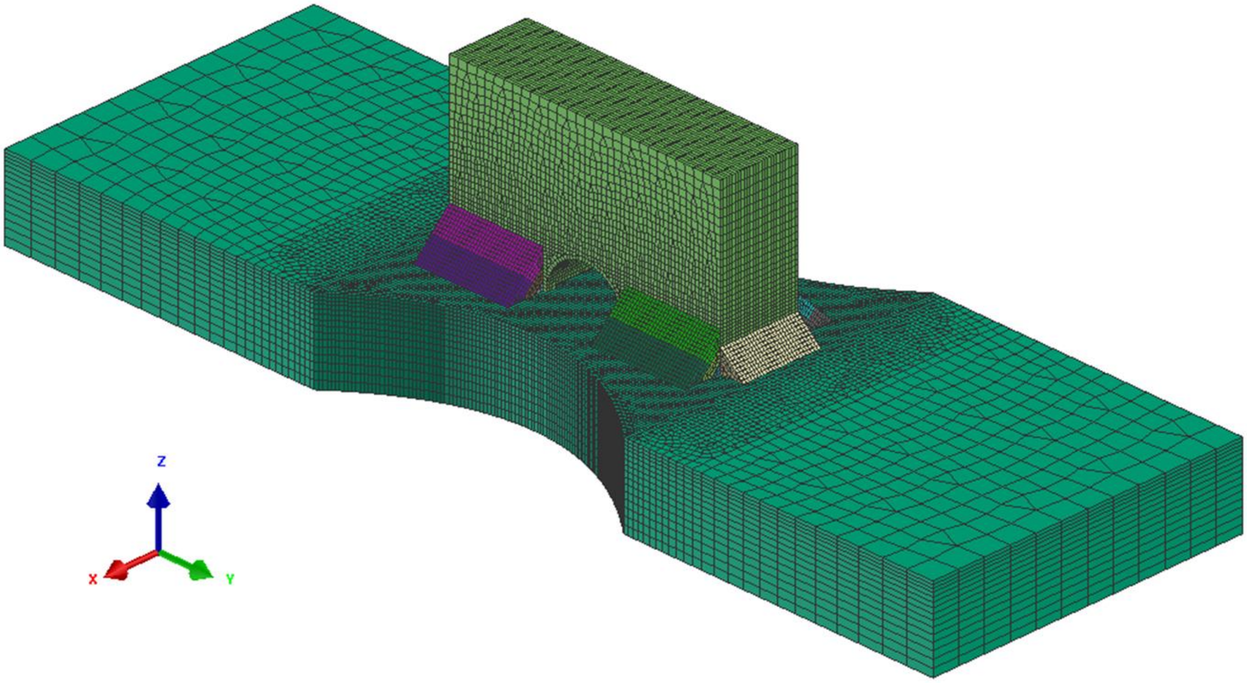

Figure 4. FEA model for the final welded component, Specimen #3.

For the *SYSWELD* model, the 3D element size near the weld area (weld beads and heat affected zone [HAZ]) was 1, corresponding with an element of less than 1 mm (0.04 in) per side. Farther away from the weld areas, the mesh was less refined to increase computational efficiency as shown in **Figure 4**. As the physical specimen did not require clamping during fabrication, only clamps needed for mathematical node fixturing during the simulation were inserted (see **Figure 6**). These did not represent any physical clamp, but instead constrain rigid body motion in the solution of the mechanical equilibrium. To prevent thermal flow through non-connected parts (i.e., between the arch and the dog-bone), a gap in the mesh was used as shown in **Figure 7**.

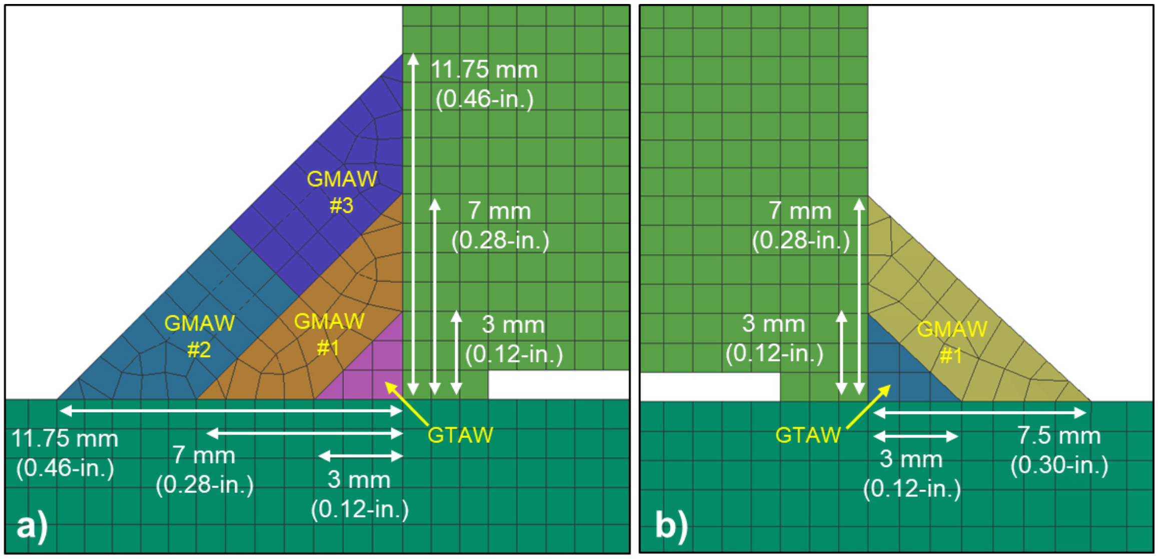

Figure 5. Weld passes showing the bead sizing and bead sequence for the **a)** longitudinal and **b)** transverse joints.

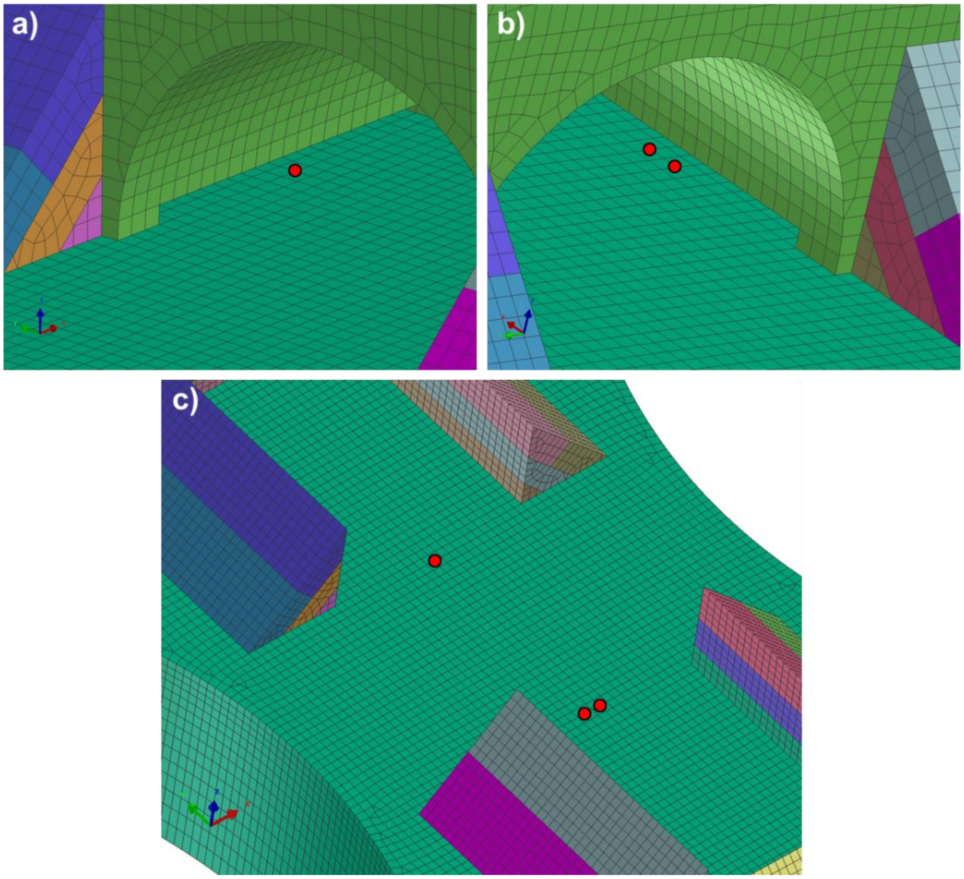

Figure 6. Clamp locations (red dots) used to represent mathematical fixturing used during the weld simulation for the **a)** single XZ clamp below one edge of the reinforcement arch, **b)** double YZ clamps below the other edge of the reinforcement arch, and **c)** all three clamps shown relative to each other with the reinforcement arch removed for clarity.

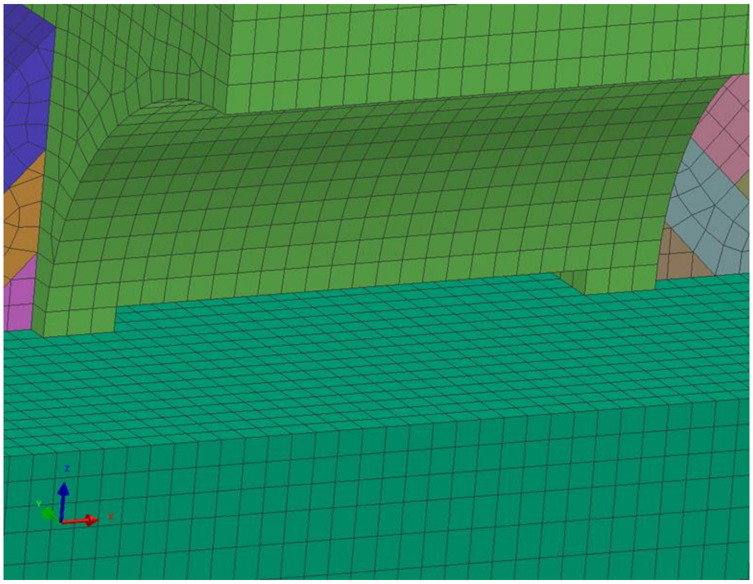

Figure 7. Non-connected surface mesh below the reinforcement arch to prevent thermal flow through a non-continuous zone in the final simulated weldment.

An average welding arc efficiency of 67% was used to mimic the GTAW passes, whereas it was 85% for the GMAW passes in accordance with reference [18]. The other welding parameters mimicked that of the physical specimen, but used average values for the welding parameters as shown in **Table 2**. The default parameters ('General Arc Welding' scenario in *Visual Weld* module) were used for the Goldak heat source parameters for the Power Ratio (1.2) and Length Ratio (0.5) of the double ellipsoid shapes. Additionally, preliminary thermal simulations facilitated V&V for the each weld pass to ensure the correct melt zone sizing for each weld pass. Correct melt zone sizing ensures the shrinkage forces were accurate during the mechanical portion of the simulation [17].

Table 2. Welding Parameters for Specimen #3 Simulation

Parameter		**GTAW**	**GMAW**
Travel Speed (mm/s [ipm])		1.2 [2.8]	4.3 [10.2]
Heat Input (J/mm [kJ/in])		250 [6.35]	1080 [27.4]
Arc Efficiency		67%	85%
Goldak Heat Source Parameters	**Length (mm) [in]**	6 [0.24]	10 [0.39]
	Width (mm) [in]	3 [0.12]	8 [0.31]
	Penetration (mm) [in]	2 [0.08]	4 [0.16]
Preheat Temperature		100 °C (212 °F)	
Interpass Temperature		93-149 °C (200-300 °F)	
Ambient Temperature	**Initial**	100 °C (212 °F)	
	Final	20 °C (68 °F)	
Time Between Beads (s)		100	
Time Between Passes (s)		1000	

As shown in **Table 2**, the timing between weld passes was 100 seconds between the start of each weld bead, but was 1000 seconds between the start of each successive weld pass (i.e., GTAW root pass #1 started at 0 seconds, GMAW cover pass #1 started at 1000 seconds, GMAW cover pass #2 at 2000 seconds, and GMAW cover pass #3 at 3000 seconds). Preliminary thermal simulations showed this timing facilitated the interpass temperature requirements.

The simulation was carried out to a time of t = 8000 seconds, which allowed the model to reach room temperature conditions and serve as the "final" state of the model. The pre-heat value from **Table 2** represents the initial temperature at which all the nodes within each *SYSWELD* simulation started. This same value, 100 °C (212 °F), was also used at the initial ambient temperature through 4000 seconds to mimic the thermal effect of continual re-heating with an oxyacetylene torch to maintain the interpass temperature of 93-149 °C (200-300 °F). At 4000 seconds, the ambient temperature was reduced to 20 °C (68 °F) to simulate the end of torch re-heating as the weldment cooled. These ambient temperature values represents the boundary condition for the outer surfaces of the simulated weldment. The radiative and convective losses were calculated using a radiation emissivity (ε_0) of 0.8 and convective heat transfer coefficient (h_c) of 25 W/m^2/K, the default values from the *Visual Weld* module software for a "free air cooling" scenario [19].

As noted in the previous section, the frame was fabricated of HSLA-100 steel with an ER100-s filler metal. However, the *SYSWELD* software did not have a material database for either of these materials at the time this project was conducted. Therefore, a material called 'TRIP 700Z' was used for both the plate and filler metal in all simulations. **Table 3** shows a comparison between the typical thermal conductivity, specific heat, and yield strength values for the base metal materials at 25°C (77°F). Note the highly similar thermal and strength properties between the HSLA-100 and TRIP 700Z steels.

Table 3. Comparison of Material Properties at Room Temperature

Material	Thermal Conductivity		Specific Heat		Yield Strength	
	W/m·K	BTU/hr·ft·°F	J/kg·K	BTU/lb·°F	MPa	ksi
HSLA-100 [12] [20]	32.8	19.0	482	0.115	>690	110
TRIP 700Z [21]	34	19.6	510	0.122	700	101.5

Strain Analysis

Measurements were performed on the structural materials beamline (SMB) at CHESS. Energy dispersive diffraction (EDD) was carried out using polychromatic (50-200 keV) x-rays. An overview of the experimental set-up is shown in **Figure 8a**. For these measurements, a single-element Canberra GL-0055 energy resolved detector was used and placed on a down-stream optical path (also referred to in this report as the detector arm) in the horizontal plane at a 2θ angle of 7.82026. The diffraction volume was defined by: a) the beam-defining slit upstream of the sample [0.2 mm (0.008-in.) horizontal by 0.5 mm (0.020-in.) vertical]; and b) two slits on the downstream detector arm with a separation distance of ~1420 mm (55.9-in.) when the first slit was 718 mm (28.3-in.) away from the sample. The diffraction volume in the horizontal plane had a through-thickness full-width at half-maximum (FWHM) of 1.08 mm (0.04-in.). The horizontal slit size was critical to establishing the through-thickness resolution, while the relatively larger vertical slit spacing increased the diffraction volume and decreased collection time for this relatively thick steel plate.

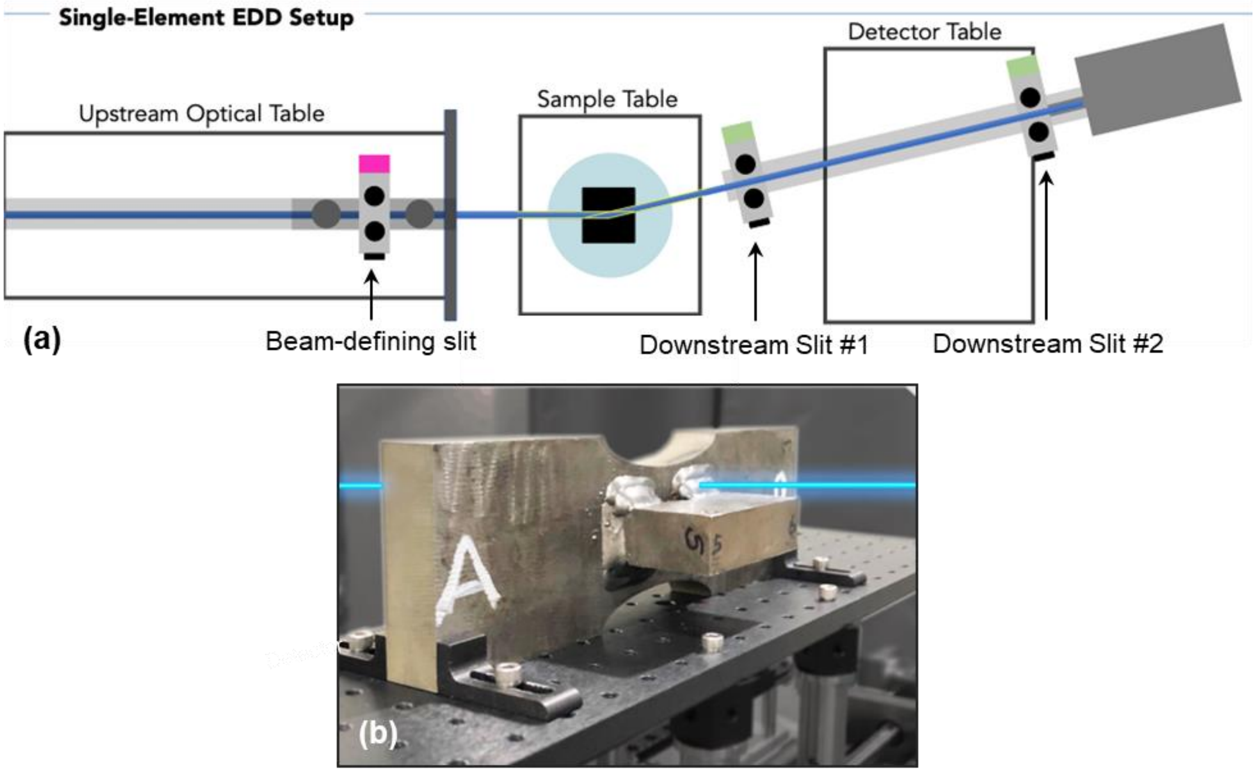

Figure 8. **a)** Overview of the EDD experimental set-up at CHESS and **b)** close-up of the welded sample on the sample table in one configuration with the direct beam-path (blue line) drawn for clarity.

For calculating the strains, the true strain was taken as:

$$\varepsilon = \ln\left(\frac{d^{(i)}}{d_0^{(i)}}\right) \quad \textbf{Eq. 1}$$

where $d_0^{(i)}$ is the reference and $d^{(i)}$ is the elastically-deformed lattice spacing for reflection. Introducing Bragg's Law, $\lambda = 2d^{(i)} \sin\hat{\theta}$, where $\hat{\theta}$ is the fixed angle from the EDD geometry, yields:

$$\varepsilon = \ln\left(\frac{\lambda_0^{(i)} \sin\hat{\theta}}{\lambda^{(i)} \sin\hat{\theta}}\right) \quad \textbf{Eq. 2}$$

Taking $E^{(i)} = 12.398/\lambda^{(i)}$, and simplifying **Equation 2** yields:

$$\varepsilon = \ln\left(\frac{E_0^{(i)}}{E^{(i)}}\right) \quad \textbf{Eq. 3}$$

Rearranging **Equation 3**, the energy based on the instantaneous value of the lattice strain (ε) is then:

$$E^{(i)} = E_0^{(i)} \exp\left(\varepsilon^{(i)}\right) \quad \textbf{Eq. 4}$$

Multiple peaks were fit simultaneously, using the least squares routine from the SciPy optimization library [22]. Optimized parameters included the peak center intensity (as energy) and shape. Calculation of the residual draws peak evaluation routines from hexrd [23]; a Gaussian peak profile was taken in the present work. A linear background correction was included and bounds are prescribed for the peak shape, such that parameters associated with a relatively weak peak are restricted from contributing to the overall background correction. Three progressive least squares optimizations were performed as described below:

1. Initial optimization using a common strain for all peaks, i, such that: $\varepsilon^{(i)} = \bar{\varepsilon}$.
2. Second optimization invoking a 'robust' least squares. The notion here is to keep a peak with relatively large intensity from dominating the residual by means of a loss function [22]. The loss function is scaled in order to separate 'weak' and 'strong' peaks. The initial parameters are taken from the prior optimization with common strain.
3. Final optimization invoking the usual least squares but using initial parameters from robust least squares optimization.

A histogram of difference between the intensity-weighted average strain from the least squares fit and common strain fit are given in **Figure 9** for the ε_{yy} component at measurement locations adjacent to the two-pass weld (location discussed in more detail below). The differences were relatively small, being less than an order of magnitude compared to the peak residual strains developed in welding.

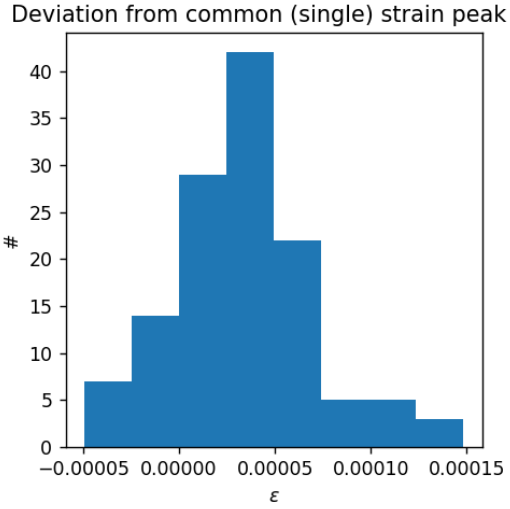

Figure 9. Distribution of difference between fit for ε_{yy} component, taking a common strain to fit peaks and average of least squares solution with distinct strain evaluated for each peak.

Lattice Parameter Verification

The zero-strain lattice parameter of the alloy was calculated and cross-checked using a series of line scans. First, a line scan of the YY strain component was performed on a high symmetry vector along the center axis of the un-welded reinforcement arch (see **Figure 2**, Plate #2), where the strain is expected to be zero along this line (see **Figure 10**). The lattice parameter was adjusted until the strain was within 1 x 10^{-6}. As a cross check, a series of scans through the thickness of the large plates – checked on Specimen #1, the dog-bone shape of Specimen #2, and the dog-bone shape of Specimen #3) were measured for the in-plane YY strain component. Assuming a biaxial stress state with balanced through-thickness tensile and compressive stresses in the rolled plate, the sum of the strains in the through-thickness direction for each line scan should be zero. The lattice parameter resulted in summed strains less than 1 x 10^{-4}, the resolution limit for the experimental conditions of this technique. Therefore, the lattice parameter of 2.8691 was determined to be reasonable. The plates were assumed to be compositionally uniform in the through-thickness direction for the purposes of this lattice parameter calibration.

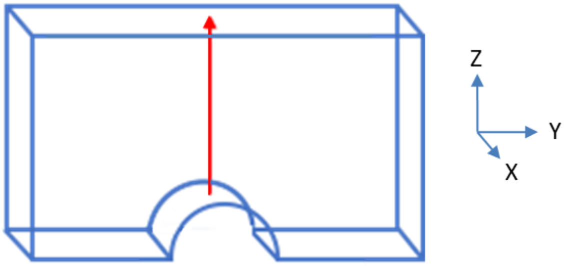

Figure 10. Geometry of calibration scan on the water-jet cut but un-welded reinforcement arch from Specimen #2. The red vector indicates the line along which the scan was performed scan.

EDD Measurement Locations

The location of the EDD measurements was at the center cross-section of two different (but representative) weld joint types – longitudinal and transverse. **Figure 11** shows section cuts of the CAD file highlighting the two different locations for the EDD measurements completed below those weld joints. This EDD data was used for V&V of the *SYSWELD* simulations.

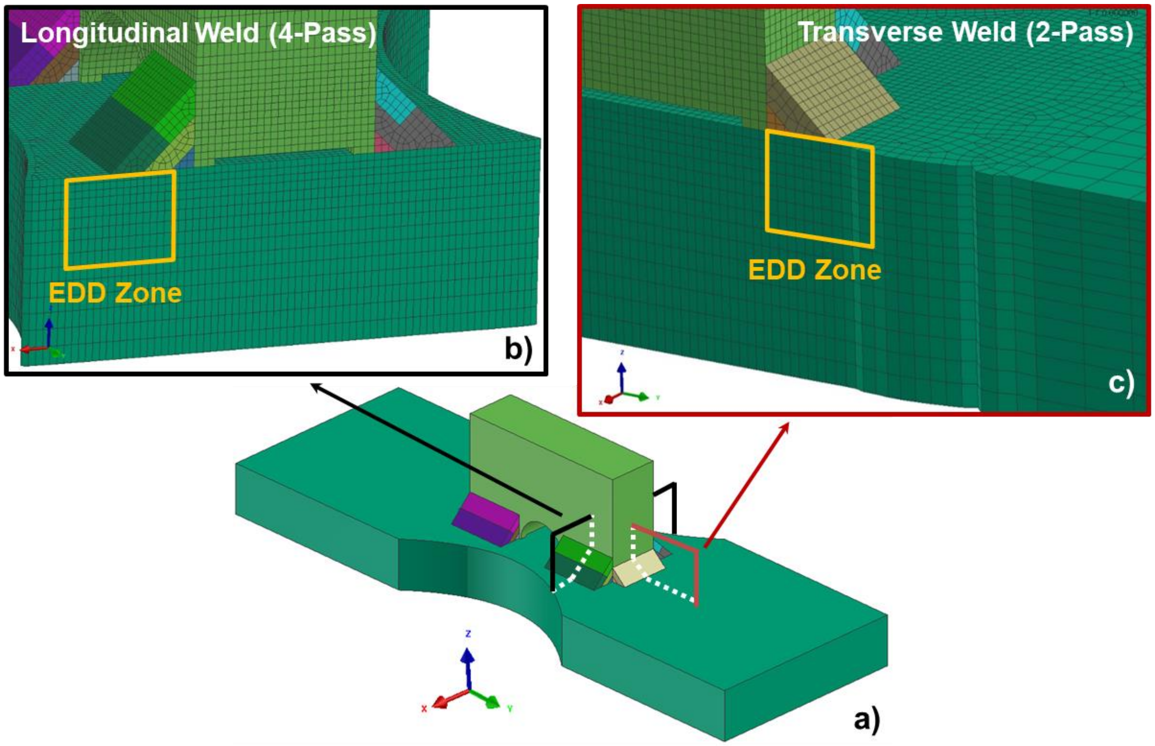

Figure 11. Image of the **a)** CAD model showing the locations of the EDD measurement zones below the **b)** longitudinal and **c)** transverse weld joints.

RESULTS AND DISCUSSION

Material Properties

Table 4 shows a comparison of the measured chemical composition to that of specifications. The reported values for all elements except for carbon and sulfur are an average of twelve measurements; carbon and sulfur values were an average of six measurements. No individual measurement fell outside the specification range for any element. **Table 5** shows the measured mechanical properties of the selected plate. There was not found to be a significant difference between the specimens tested longitudinally versus transverse in relation to the length of the plate. The HSLA-100 plate was found to meet the specified requirements in Tech Pub 300 [12].

Table 4. Chemical Composition of HSLA-100 Plate (wt%)

Type	C	Mn	Si	Ni	Cr	Mo	Cu
Measured	0.05	0.88	0.24	1.71	0.60	0.32	1.15
Specification	<0.06	0.75-1.15	<0.40	1.50-2.00	0.45-0.75	0.30-0.55	1.00-1.30

Type	P	S	Nb	Al	Ti	V	Sn	Fe
Measured	0.008	0.003	0.03	0.019	0.016	0.00	0.022	Bal.
Specification	<0.020	<0.004	0.02-0.06	>0.010	<0.02	<0.03	<0.030	Bal.

Table 5. Mechanical Properties of HSLA-100 Plate

Longitudinal Specimen	#1	#2	#3	#4	Avg. ± 1σ
Elastic Modulus (GPa)	202.7	195.8	200.6	201.3	200.1 ± 3.0
Yield Strength (MPa)	717.7	704.6	711.5	703.3	709.3 ± 6.7
Tensile Strength (MPa)	778.4	772.2	775.0	768.8	773.6 ± 4.1
Elongation (%)	25	25	25	25	25.0 ± 0
Transverse Specimen	**#5**	**#6**	**#7**	**#8**	**Avg. ± 1σ**
Elastic Modulus (GPa)	211.7	204.8	206.2	204.1	206.7 ± 3.4
Yield Strength (MPa)	707.4	725.3	710.2	717.1	715.0 ± 8.0
Tensile Strength (MPa)	772.9	783.9	772.2	781.2	777.6 ± 5.9
Elongation (%)	25	25	25	25	25.0 ± 0

Representative Weld Cross-Sections

Figure 12 shows the cross-sections of the representative weld passes used for weld bead sizing during the FEA simulations. As expected, the GMAW covering passes were found to thermally overwhelm the GTAW root pass. Additionally, the penetration depth of each weld pass (particularly the first GMAW pass) helped to understand which elements to connect between the reinforcement arch and dog-bone shape in the FEA model. It should be noted that the transverse joints only had a root GTAW pass and covering GMAW pass, as shown in **Figure 12b**, whereas the longitudinal joints had the root GTAW pass and three covering GMAW passes, as shown in **Figure 12c**.

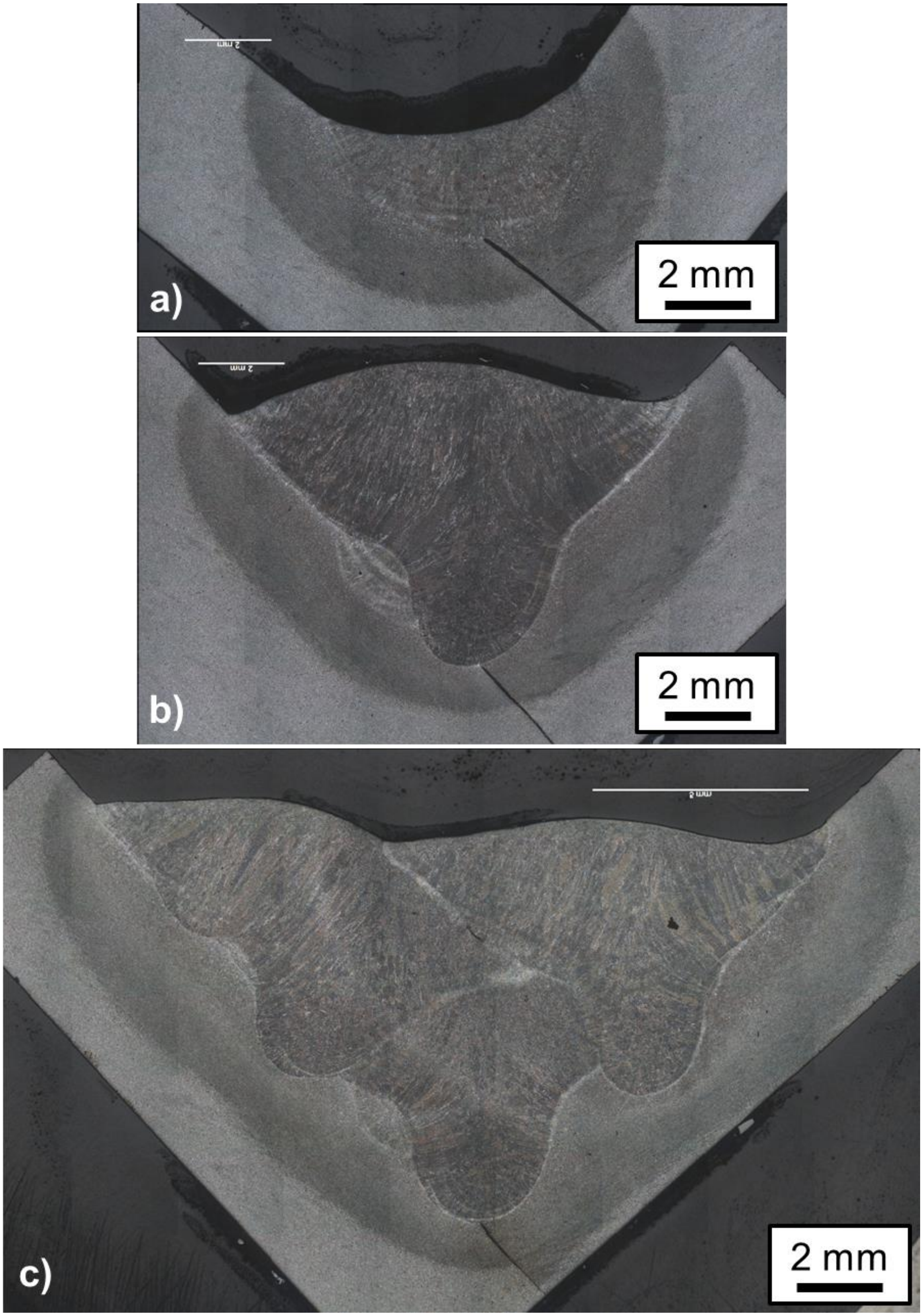

Figure 12. Representative cross-sections of the different joint conditions for weld bead size comparison of the **a)** GTAW root pass, **b)** GTAW root pass and GMAW cover pass, and **c)** GTAW root pass and three GMAW cover passes.

Weldment Fabrication

Fabrication of the thick-plate weldment involved several steps, shown in **Figure 13**. First, the sides of the reinforcement arch and the assigned "top" of the dog-bone were ground to clean metal. Second, four GTAW tack welds to hold the reinforcement arch in place on the dog-bone shape. Next, the GTAW pass for each longitudinal and transverse joint followed by the GMAW cover pass for each longitudinal and transverse joint. Lastly, the additional two GMAW cover passes for each longitudinal joint. The longitudinal and transverse weld beads were kept as separated as possible, but due to fluid flow to complete the end of weld beads, some overlap did occur at the edges (see black arrows in **Figure 13c-d**). These "connections" were ignored for the subsequent welding simulations.

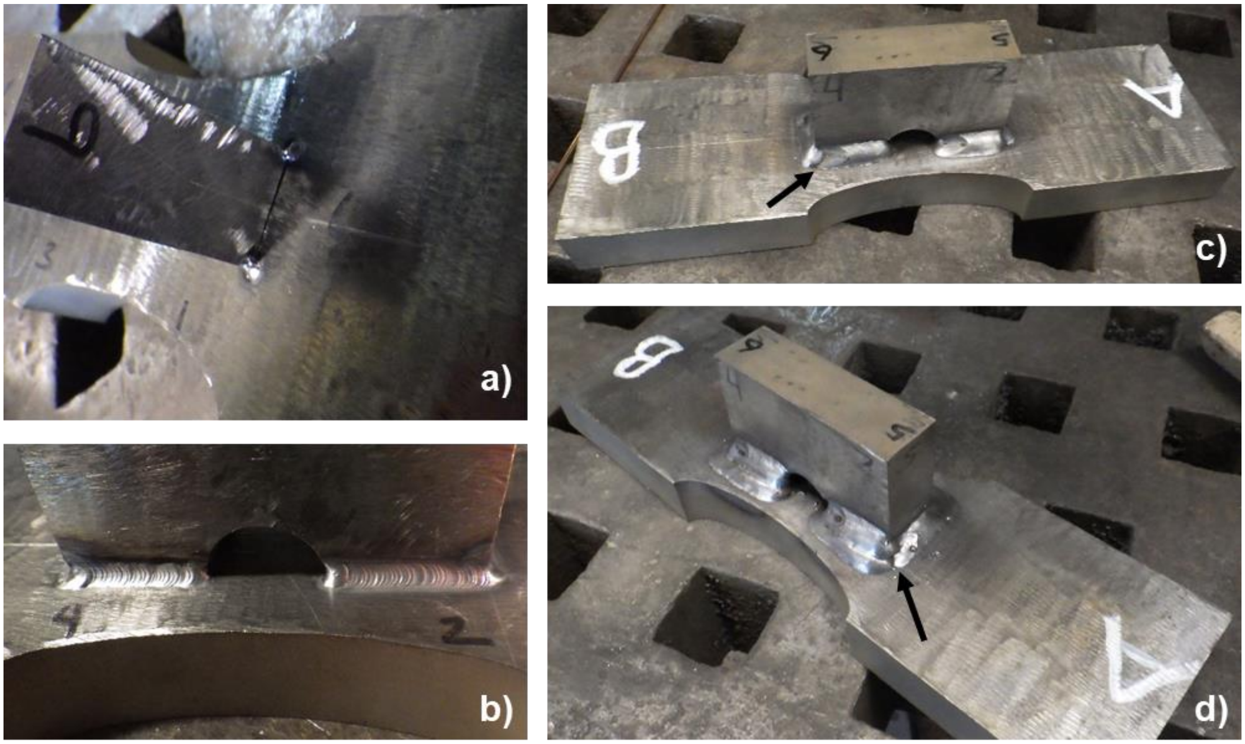

Figure 13. Images of the different welding steps for Specimen #3, including: **a)** the GTAW tack welds on each corner of the reinforcement arch, **b)** the GTAW root pass on all longitudinal and transverse joints, **c)** the GMAW cover pass on all longitudinal and transverse joints, and **d)** the additional two GMAW cover passes on all longitudinal joints.

As expected in the thick-plate (nominally 25.4 mm [1-in.]) weldment, there was little distortion noted. The most was a slight curvature, below 1 mm (0.04-in.), found in the dog-bone shape of Specimen #3 post-welding as shown in **Figure 14**. However, this slight lack of flatness was not found in the Specimen #2 cut shapes (dog-bone and arch) but was noted in Specimen #1 (incoming plate). This leads the authors to believe the non-flatness has origins in initial plate production, which was not included in the FEA simulations at this time. Follow-on work will investigate the effect of rolling and heat-treatment on the incoming FEA model used in welding simulation. However, because of the variability in the industrial processes, the author's believe the sister sample examination is valid to determine the trends across the fabrication process, despite any slight imprecision the lack of initial plate fabrication information (distortion and stress) that can be included in the welding simulation at this time.

Figure 14. Image of the slight curvature (less than 1 mm [0.04-in.]) found in dog-bone shape portion of Specimen #3 post-welding.

Computational Simulation

The *SYSWELD* simulations resulted in several thermo-physical and thermo-mechanical datasets that validated results from the physical fabrication. **Figure 15** shows the representative images of the melt pool for each weld pass condition at the center cross-section of the bead exhibiting the largest melt pool. It was found that the melt pool did not significantly change between the different beads at different locations on the weldment. This was expected due to the average welding parameters used during the FEA simulation. The melt pool sizes shown in **Figure 15** matched the expected weld bead width and penetrations shown in **Figure 12**, which validates the simulation technique according to AWS A9.5 standards [17]. **Figure 16** shows the maximum temperature realized at every node throughout the entire simulation, highlighting that the entire weld zone was melted. The reverse side of the weldment exhibited similar thermal profiles. The thermal simulations also verified that the interpass temperature, 93-149 °C (200-300 °F), was maintained throughout the welding process, which matches that of the physical fabrication of Specimen #3. The highest temperature for any node at the completion of the entire simulation (8000 seconds) was 22.9 °C (73.2 °F).

The FEA simulation results predicted there would be less than 0.52 mm (0.02-in.) distortion for any node at the completion of the simulation, as shown in **Figure 17**. Further examination showed that no node exhibited any additional distortion above 0.7 mm (0.03-in.) at any point within the entire weld simulation. The as-expected lack of distortion also serves as V&V for the simulation compared to the physical specimen, which also yielded little distortion as shown in **Figure 14**.

The FEA simulation results predicted the highest residual stress near the weldments, as shown in **Figure 18**. Similar stress states were predicted for the reverse side of the weldment. A peak value of 700-750 MPa (102-109 ksi) was selected because the minimum yield strength of HSLA-100 plate material is 690 MPa (100 ksi). **Figure 19** shows additional images of cross-sections at the mid-point of the different weld joints, both longitudinal and transverse. As expected, the highest stress zones were found to be near the root of each welded joint.

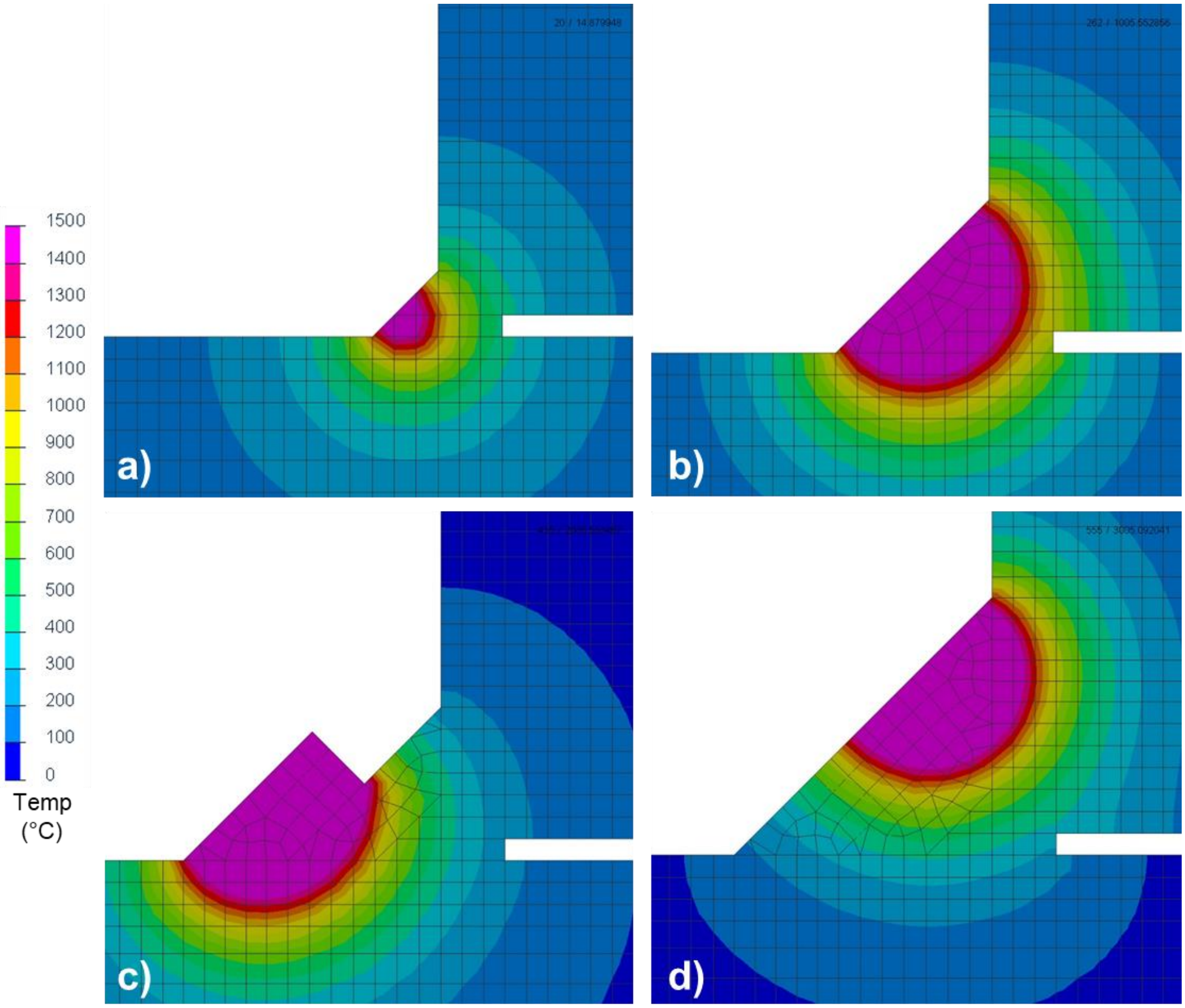

Figure 15. Representative *SYSWELD* images showing cross-sections of the weld pool temperature for each weld condition, including **a)** GTAW root pass, **b)** first GMAW cover pass, **c)** second GMAW cover pass, and **d)** third GMAW cover pass. Note the pink color shows the melt zone based on the peak temperature reached, name above 1400 °C (2552 °F).

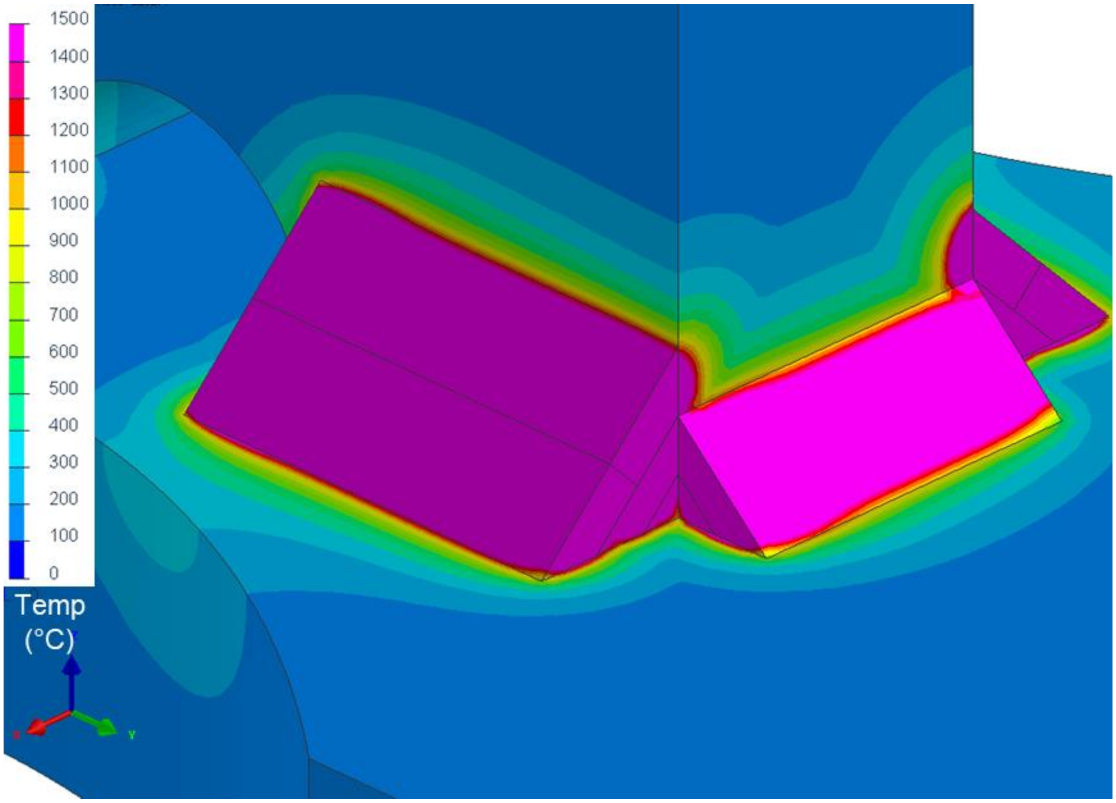

Figure 16. Representative *SYSWELD* image showing the maximum temperature reached throughout the entire welding simulation. Note the pink color shows the melt zone based on the peak temperature reached, name above 1400 °C (2552 °F).

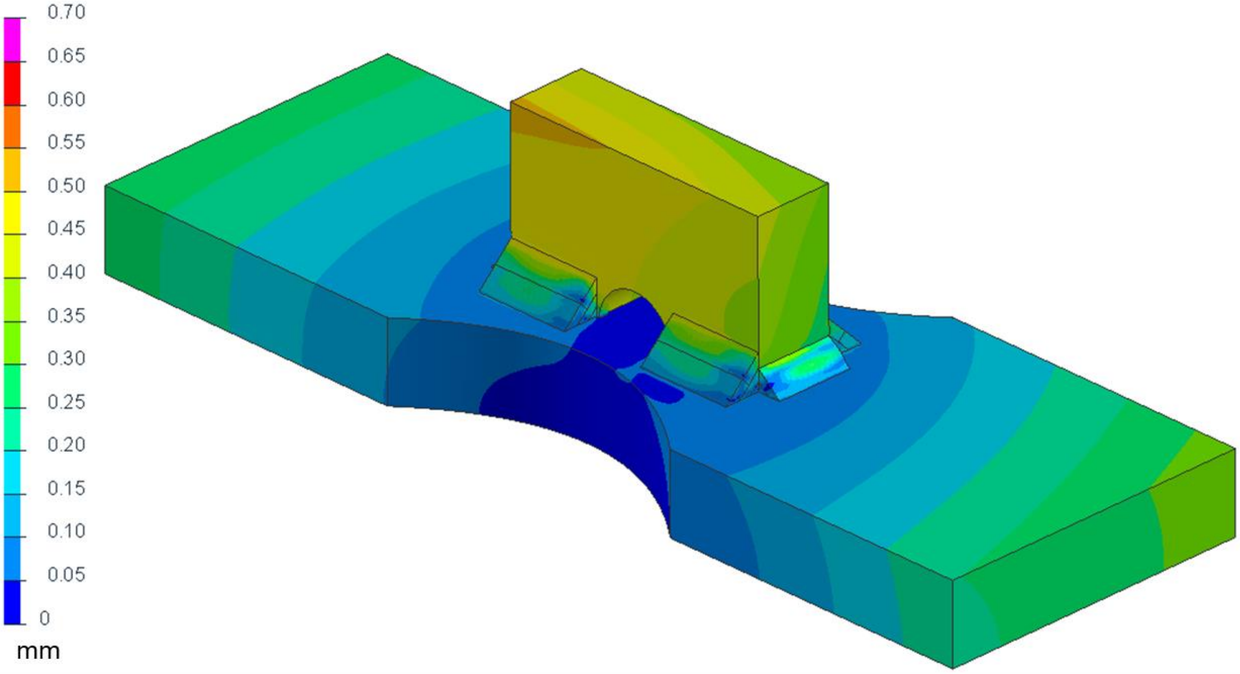

Figure 17. S*YSWELD* image of the final distortion state of the weldment after the completion of welding and the cooling period to bring the piece back to room temperature.

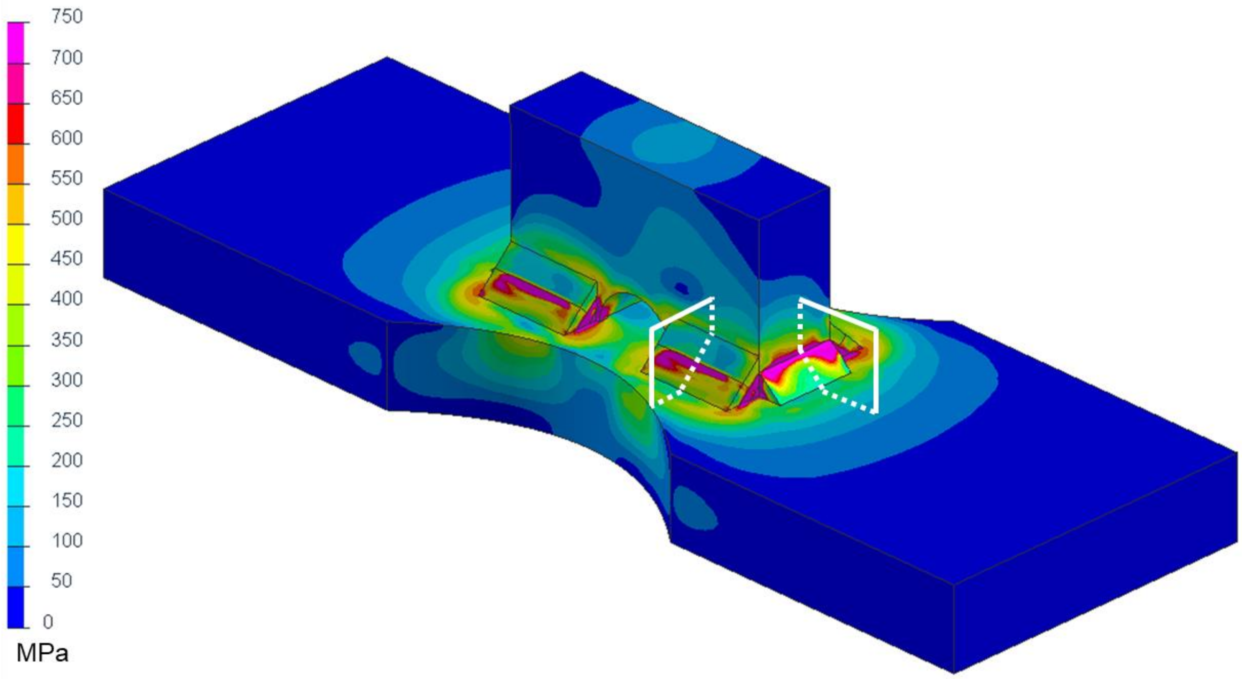

Figure 18. S*YSWELD* image of the final stress state (Von Mises criteria) of the weldment after the completion of welding and the cooling period to bring the piece back to room temperature. Note the white shapes designate the specific joint cross-sections of the longitudinal and transverse welds shown in **Figure 19-Figure 21**.

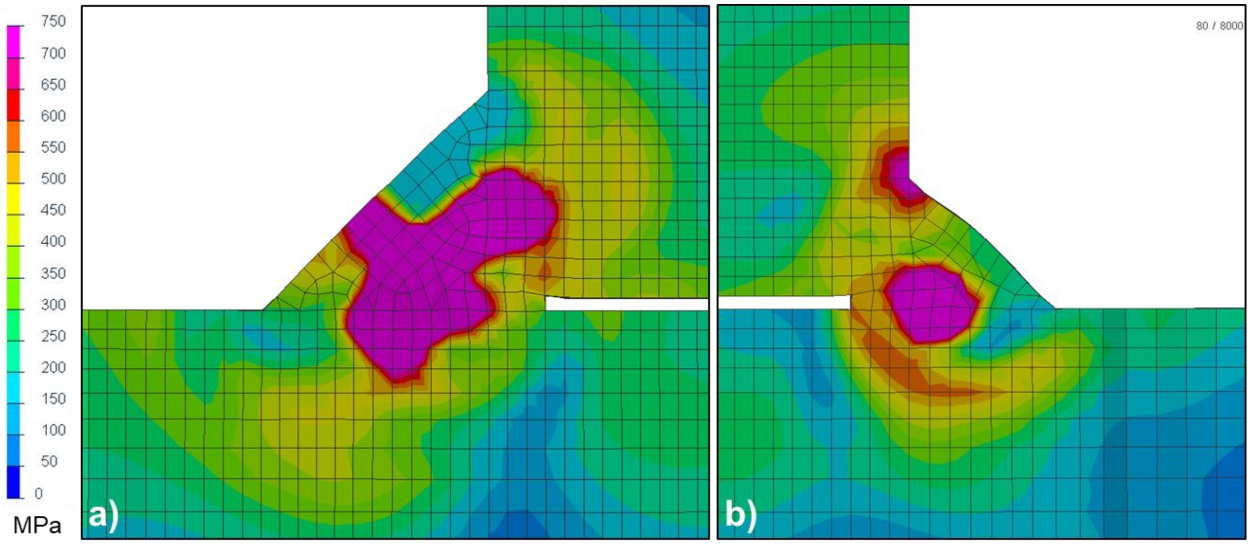

Figure 19. Representative *SYSWELD* images showing cross-sections of the final stress state (Von Mises criteria) for the **a)** longitudinal and **b)** transverse joints.

For comparison to the X-ray measurements from CHESS, an examination of the residual stress across the six principle stress directions (XX, YY, ZZ, XY, XZ, YZ) was needed. **Figure 20** shows these results for the longitudinal (4-pass) weld joint, whereas **Figure 21** shows the results for the transverse (2-pass) weld joints. Note that the first principle stress values were predicted to be relatively consistent across the symmetric planes of the weldment, so only one representative cross-section is shown for each weld joint condition.

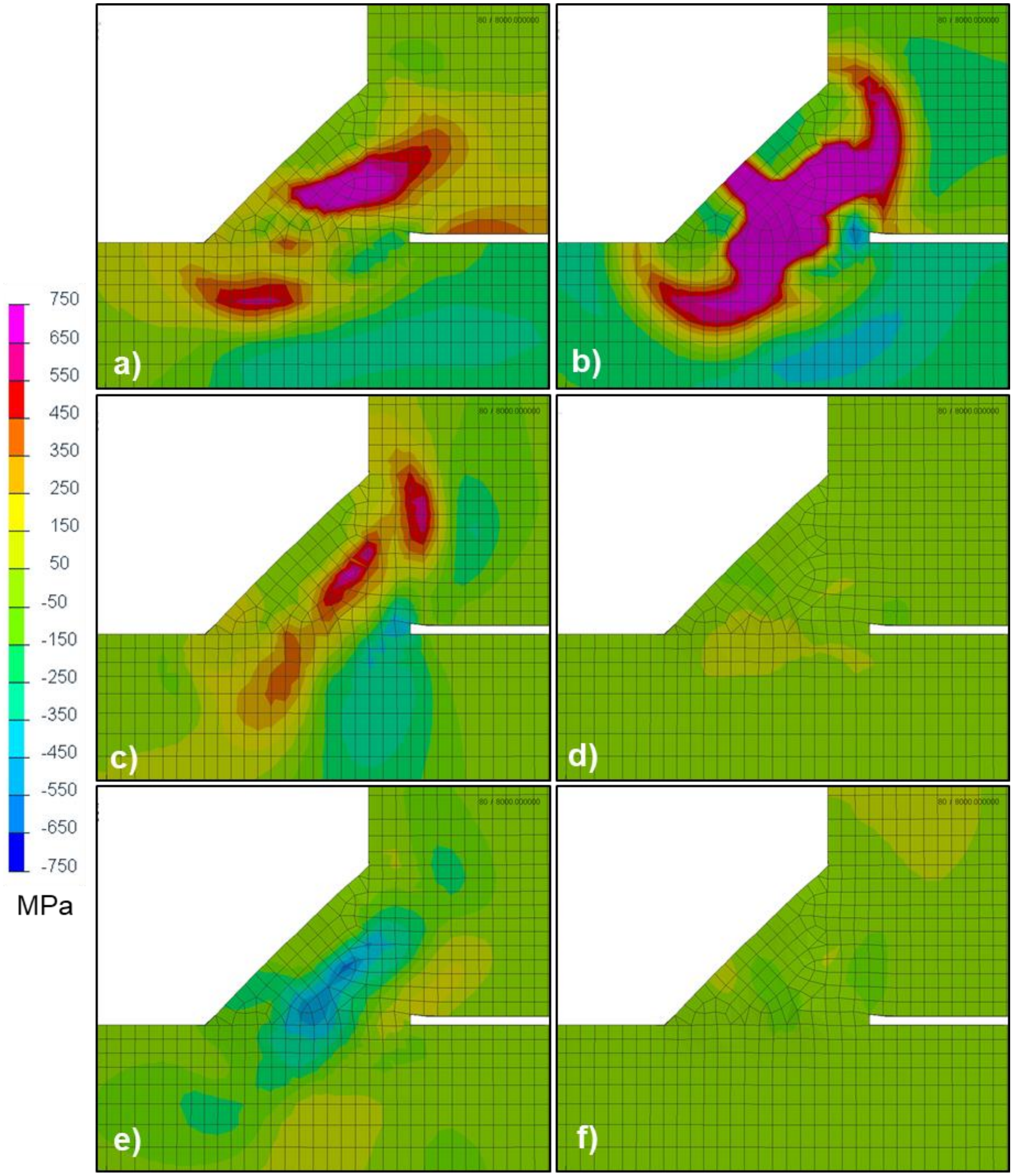

Figure 20. Representative *SYSWELD* images showing cross-sections of the final first principle stress state for the longitudinal (4-pass) weld joint scenario for all directions: **a)** XX, **b)** YY, **b)** ZZ, **d)** XY, **e)** XZ, **f)** YZ.

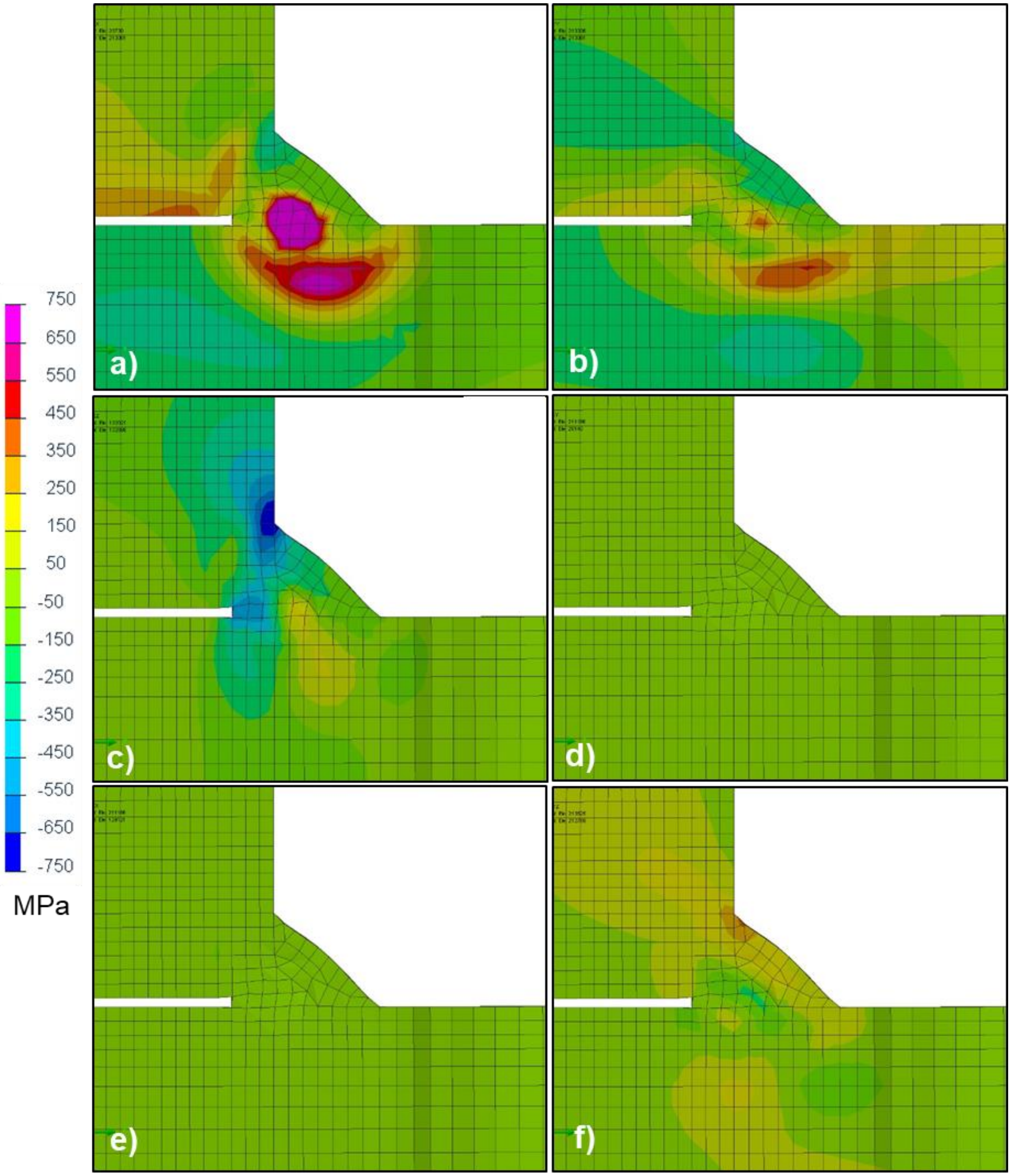

Figure 21. Representative *SYSWELD* images showing cross-sections of the final first principle stress state for the transverse (2-weld) weld joint scenario for all directions: **a)** XX, **b)** YY, **b)** ZZ, **d)** XY, **e)** XZ, **f)** YZ.

Strain Measurement and Comparison

Strain components measured through EDD are shown as contour maps for two strain components (ε_{xx} and ε_{yy}) orthogonal to the weldment dimensions. **Figure 22** shows these results for the longitudinal (4-pass) weld joint in ε_{xx}, **Figure 23** shows the longitudinal (4-pass) weld joint in ε_{yy}, **Figure 24** shows the transverse (2-pass) weld joint in ε_{xx}, and **Figure 25** shows the transverse (2-pass) weld joint in ε_{yy}. The coordinate system for the EDD measurements matched that of the simulated weldment, as shown in **Figure 4**. In **Figure 22-Figure 25**, the circle symbols in each EDD plot represent the specific positions of the EDD measurements and are colored by their direct strain measurement. The contours between each circle are interpolated using the location-specific data at each EDD measurement point. For clarity of comparison, the black box in the *SYSWELD* simulation data maps represents the area where the EDD measurements were taken for clarity of comparison, whereas the dashed outline of shapes above the *SYSWELD* simulation data maps show the relative location of the individual GTAW and GMAW passes for each joint scenario.

The *SYSWELD* simulation strains for the derived maps in **Figure 22-Figure 25** were calculated from the predicted first principle stress tensor (XX, YY, ZZ, XY, XZ, and YZ) at each node. Maps of those stress values were shown previously for both weld joint configurations in **Figure 20-Figure 21**. The predicted nodal stress (σ) was converted to strain (ε) using the isotropic form of Hooke's law:

$$\varepsilon_{ij} = \frac{1}{E}\left[\sigma_{ij} - v\left(\sigma_{kk}\delta_{ij} - \sigma_{ij}\right)\right] \qquad \textbf{Eq. 5}$$

where *i*, *j*, and *k* = directions in x,y,z space, *E* = elastic modulus (taken as 210 GPa [30.4 Msi] for steel), *v* = Poisson's ratio (taken as 0.33 for steel), and δ = Kronecker delta (either 0 or 1).

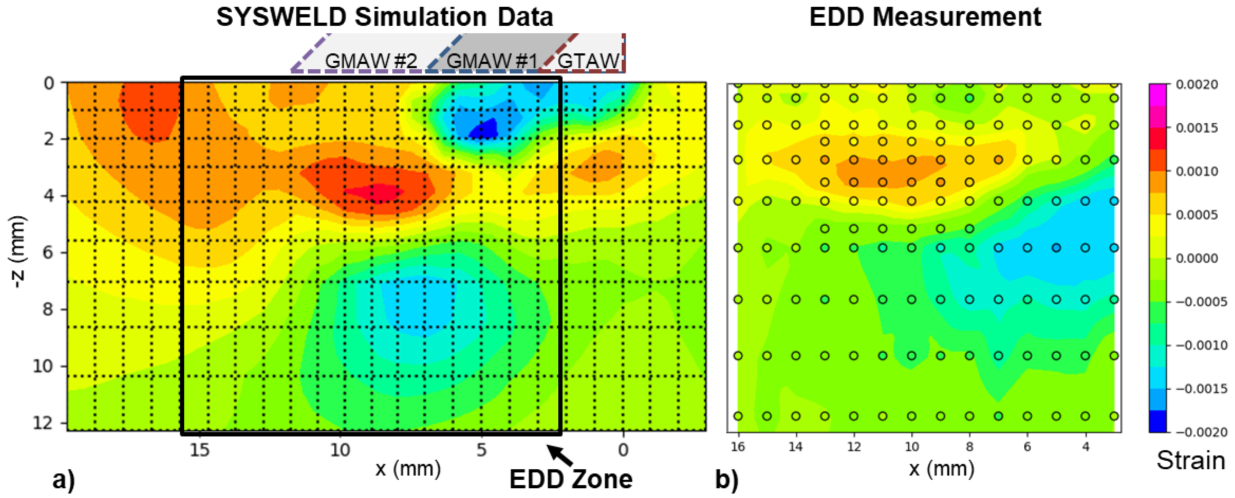

Figure 22. Comparison of strain map in the XX direction for the cross-section of the longitudinal (4-weld) joint for **a)** the calculated *SYSWELD* strain map compared to **b)** the EDD measurement strain map. The black box on the left image shows the area on the *SYSWELD* strain map where the EDD measurements were taken.

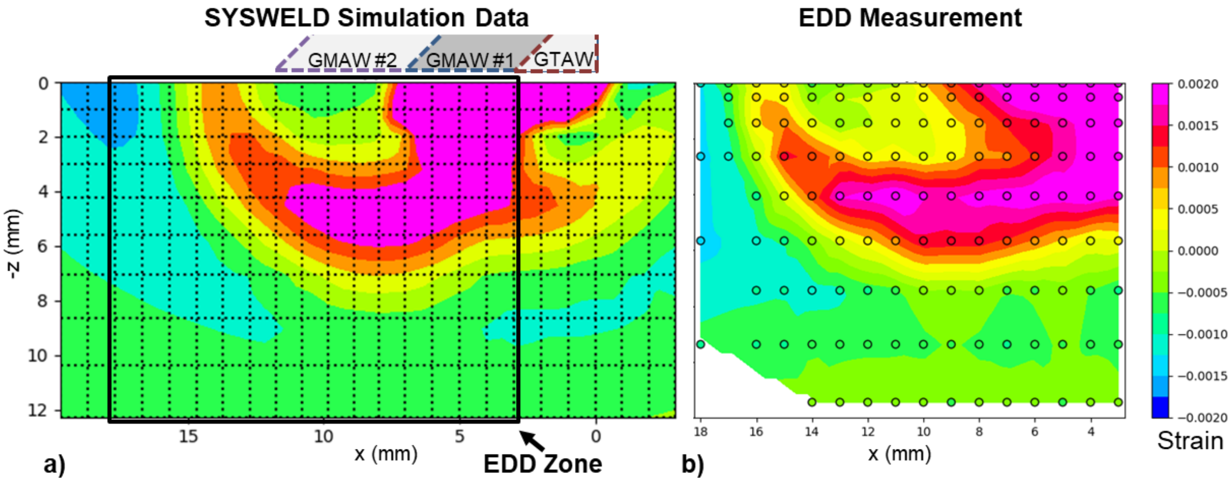

Figure 23. Comparison of strain map in the YY direction for the cross-section of the longitudinal (4-weld) joint for **a)** the calculated *SYSWELD* strain map compared to **b)** the EDD measurement strain map. The black box on the left image shows the area on the *SYSWELD* strain map where the EDD measurements were taken.

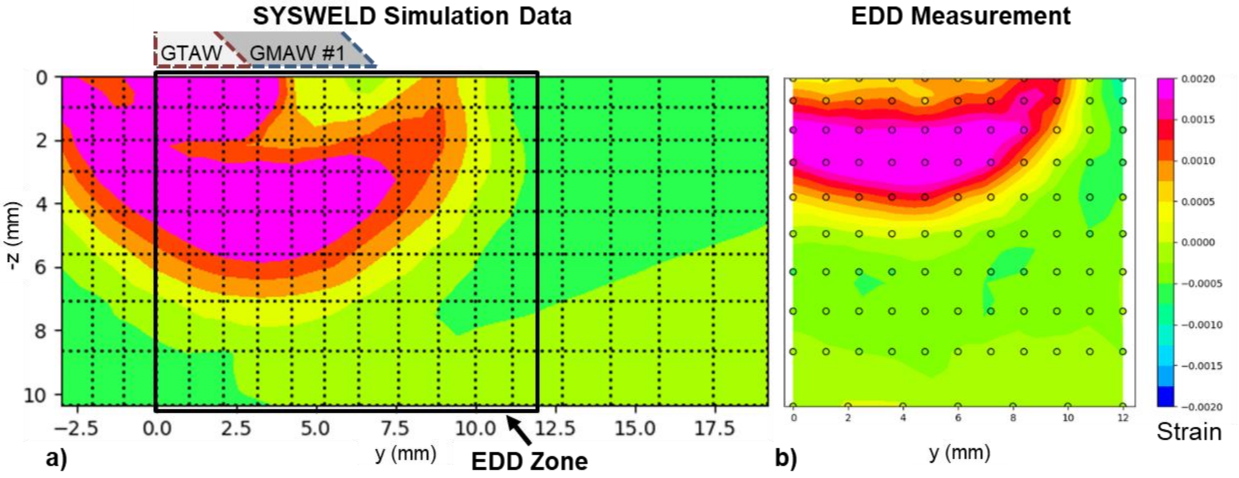

Figure 24. Comparison of strain map in the XX direction for the cross-section of the transverse (2-weld) joint for **a)** the calculated *SYSWELD* strain map compared to **b)** the EDD measurement strain map. The black box on the left image shows the area on the *SYSWELD* strain map where the EDD measurements were taken.

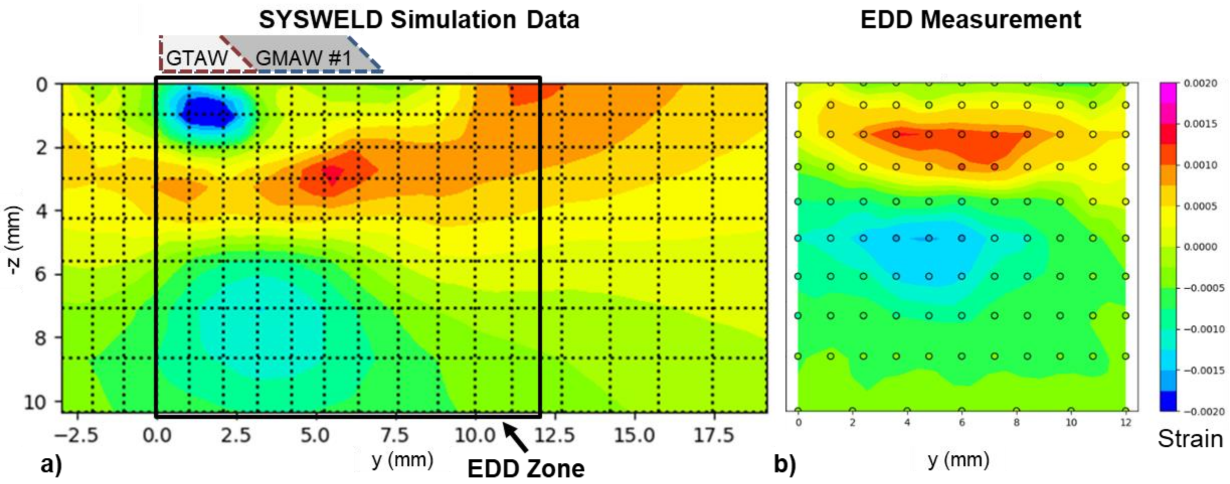

Figure 25. Comparison of strain map in the YY direction for the cross-section of the transverse (2-weld) joint for **a)** the calculated *SYSWELD* strain map compared to **b)** the EDD measurement strain map. The black box on the left image shows the area on the *SYSWELD* strain map where the EDD measurements were taken.

The predicted strain from the FEA simulation to the EDD measurements was found to exhibit high correlation for all four scenarios. In particular, the shape and curvature correlation for ε_{yy} of the longitudinal (4-weld) joint (**Figure 23**) and ε_{xx} of the transverse (2-weld) joint (**Figure 24**) showed that the highest strain levels (>0.0015) were being captured appropriately. These high tensile strains were likely caused by the shrinkage forces from weld metal solidification parallel to the welding direction of each joint and were expected. These high tensile strains were also likely to overwhelm any steel fabrication strains which evolved from the plate rolling, heat treatment, and cutting operations prior to welding, thus resulting in the best correlation between the FEA predictions and EDD measurements for those two scenarios.

While there was good agreement between the highest strain zones in the ε_{xx} of the longitudinal (4-weld) joint (**Figure 22**) and ε_{yy} of the transverse (2-weld) joint (**Figure 25**), the highest strains (>0.0015) were not realized. This is likely because these cross-sections ran orthogonal to the welding direction at each joint, and would have experienced much lower shrinkage forces. It was noted that a high compressive strain (>-0.0015) was predicted immediately beneath the weld beads within the heat-affected zone (HAZ). However, the EDD measurements did not exhibit the same localized compression strain region. The authors believe this was the result of the modified chemistry from dilution of the filler metal into the base metal within the HAZ, which would result in a slight deviation in the d-spacing for that region relative to the rest of the steel plate. Further analysis is on-going.

Other minor differences between the EDD measurements and the FEA predictions are attributed to the lack of fabrication process (*i.e.*, plate rolling, heat treatment, and cutting) information able to be inserted into the FEA simulation as of this writing. Follow-on work to examine the stress state of the incoming plate, to include the effects of the fabrication process, is on-going. A similar examination of EDD measurements compared to FEA simulations of in-coming plate and the effects of each fabrication step is on-going.

CONCLUSIONS

This materials-informed digital twin effort leveraging ICME techniques seeks to serve as the basis for inclusion of materials processing data into structural evaluation and mechanical performance. A set of “sister-samples” to represent various steps in the fabrication process was produced from a single plate of 25.4 mm (1-in.) thick HSLA-100 steel. Specimen #1 represented incoming rolled plate, Specimen #2 represented cut pieces, and Specimen #3 represented the final welded structure. Long-term efforts seek to understand the evolution and distribution of residual stress from the entire fabrication process through FEA simulations and EDD measurements, but this report focused only on data associated with the final weldment, Specimen #3.

Initial FEA analysis of the weldment showed high tensile stresses near the weld passes in the heat-affected zone (HAZ), as expected. Validation of the predicted strain within the dog-bone shape showed high correlation between the measured EDD data and the FEA predictions, particularly for the high strain (>0.0015) fields of first principle strain vectors measured parallel to each welding pass. These high strains are likely the result of the shrinkage forces associated with weld metal solidification and cooling. Follow-on work will investigate the inclusion of other fabrication-based strains (*i.e.*, plate rolling, heat treatment, and cutting) into the FEA analysis, plus establish the mechanical performance (*e.g.*, fatigue) of the final weldment in comparison to FEA analysis with and without the included fabrication stresses.

REFERENCES

[1] F. Lawrence, J. Burk and J. Yung, "Influence of Residual Stress on the Predicted Fatigue Life of Weldments," in *Residual Stress Effects in Fatigue (ASTM STP 776),* West Conshohocken, PA, ASTM International, 1982, pp. 33-43.

[2] G. A. Webster and A. N. Ezeilo, "Residual Stress Distributions and Their Influence on Fatigue Lifetimes," *International Journal of Fatigue,* vol. 23, pp. S375-S383, 2001.

[3] Z. Barsoum and I. Barsoum, "Residual stress effects on fatigue life of welded structures using LEFM," *Engineering Failure Analysis,* vol. 16, no. 1, pp. 449-467, 2009.

[4] T. D. Huang, P. Dong, L. Decan, D. Harwig and R. Kumar, "Fabrication and Engineering Technology for Lightweight Ship Structures, Part 1: Distortions and Residual Stresses in Panel Fabrication," *Journal of Ship Production,* vol. 20, no. 1, pp. 43-59, 2004.

[5] Comittee on Integrated Computational Materials Engineering - National Research Council, "Integrated Computational Materials Engineering: A Transformative Discipline for Improved Competitiveness and National Security," National Academies Press, Washington, D.C., 2008.

[6] "Integrated Computational Materials Engineering (ICME): Implementing ICME in the Aerospace, Automotice, and Maritime Industries," The Minerals, Metals, and Materials Society (TMS), Warrendale, PA, 2013.

[7] J. C. Mach, C. J. Budrow, D. C. Pagan, J. P. Ruff, J. -S. Park, J. Okasinski, A. J. Beaudoin and M. P. Miller, "Validating a Model for Welding Induced Residual Stress Using High-Energy X-Ray Diffraction," *JOM,* vol. 69, no. 5, pp. 893-899, 2017.

[8] J. C. Mach, C. Gales, J. -S. Park, J. Okasinski, C. J. Budrow, A. J. Beaudoin, K. Swartz, M. P. Miller and T. Gnaupel-Herold, "FD&E Total Life T-Sample Residual Stress Analytical Predictions and Measured Results," SAE Technical Paper, 2019.

[9] M. B. Prime, "Residual Stresses Measured in Quenched HSLA-100 Steel Plate," *Proceedings of the SEM Annual Conference and Exposition on Experimental and Applied Mechanics,* 2005.

[10] A. Bahadur, B. R. Kumar and S. G. Chowdhury, "Effect of Thermomechanical Treatment on X-Ray Elastic Constants and Residual Stresses in HSLA-100 Steel," *Journal of Nondestructive Evaluation,* vol. 22, no. 2, pp. 53-62, 2005.

[11] J. E. Duch and J. N. DuPont, "Effect of Multiple Weld Thermal Cycles on HSLA-100 Steel The Microstructure and Mechanical Properties of High-Strength Low-Alloy Steel during Multipass Welding," *Welding Journal,* vol. 98, no. 3, pp. 88S-98S, 2019.

[12] NAVSEA T9074-BD-GIB-010/300 (Rev. 2), "Base Materials for Critical Applications: Requirements for Low Alloy Steel Plate, Forgings, Castings, Shapes, Bars, and Heads of HY-80/100/130 and HSLA-80/100," NAVSEA, Washington, D.C., 2012.

[13] ASTM E417-17, "Standard Test Method for Anlaysis of Carbon and Low-Alloy Steel by Spark Atomic Emission Spectrometry," ASTM International, West Conshohocken, PA, 2017.

[14] ASTM E1019-18, "Standard Test Methods for Determination of Carbon, Sulfur, Nitrogen, and Oxygen in Steel, Iron, Nickel, and Cobalt Alloys by Various Combustion and Inert Gas Fusion Techniques," ASTM International, West Conshohocken, PA, 2018.

[15] ASTM A370-18, "Standard Test Methods and Definitions for Mechanical Testing of Steel Products," ASTM International, West Conshohocken, PA, 2018.

[16] J. Goldak, A. Chakravarti and M. Bibby, "A New Finite Element Model for Welding Heat Sources," *Metallurgical Transactions B,* vol. 15, pp. 299-305, 1984.

[17] AWS A9.5, "Guide for Verification and Validation in Computational Weld Mechanics," American Welding Society, Miami, FL, 2013.

[18] J. DuPont and A. Marder, "Thermal Efficiency of Arc Welding Processes," *Welding Journal,* vol. 74, no. 12, pp. 406-416-s, 1995.

[19] ESI Software, "Visual Weld 14.5," Accessed: 6 September 2019.

[20] Z. Hu, "Material Property Measurement for HSLA-100," 2005.

[21] Visual Environment 14.5, "TRIP 700Z," ESI Material Database, 2019.

[22] P. Virtanen, R. Gommers, T. Oliphant, M. Haverland, T. Reddy, D. Cournapeau and 1.0 SciPy Contributers, "SciPy 1.0: Fundamental Algorithms for Scientific Computing in Python," *Nature Methods,* vol. 17, p. 261–272, 2020.

[23] J. Vernier, "HEXRD," [Online]. Available: https://github.com/joelvbernier/hexrd.git.

[24] N. Yurioka, S. Oshita and H. Tamehiro, "Determination of Necessary Preheating Temperature in Steel Welding," *Welding Journal,* vol. 52, no. 6, pp. 147-s to 153-s, 1983.

APPENDIX A: Cutting Diagrams

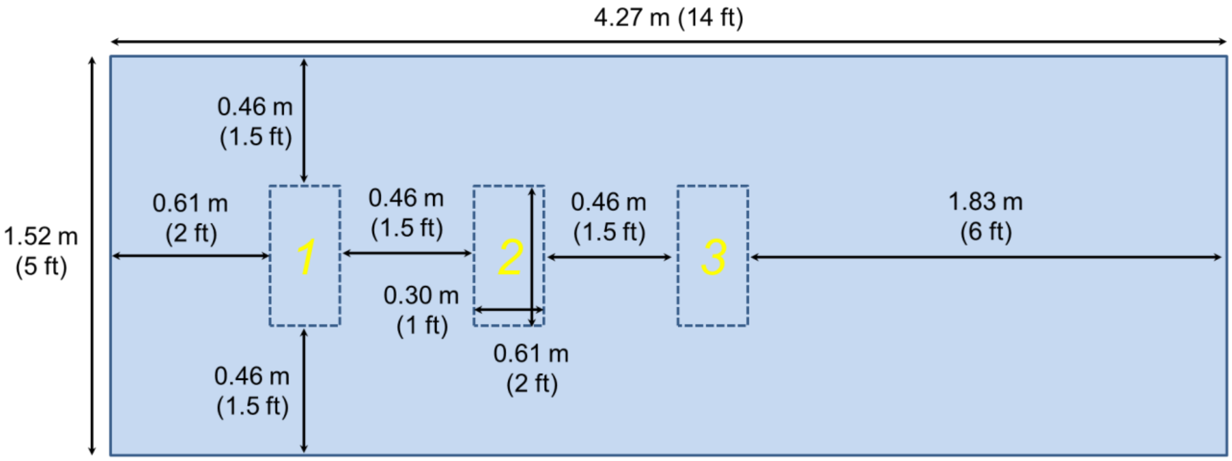

Figure A1. Schematic of the cutting diagram for the 25.4 mm (1-in.) thick plate of HSLA-100 steel showing the location of the sub-plates removed by water-jet cutting to serve as the three "sister samples" for the project.

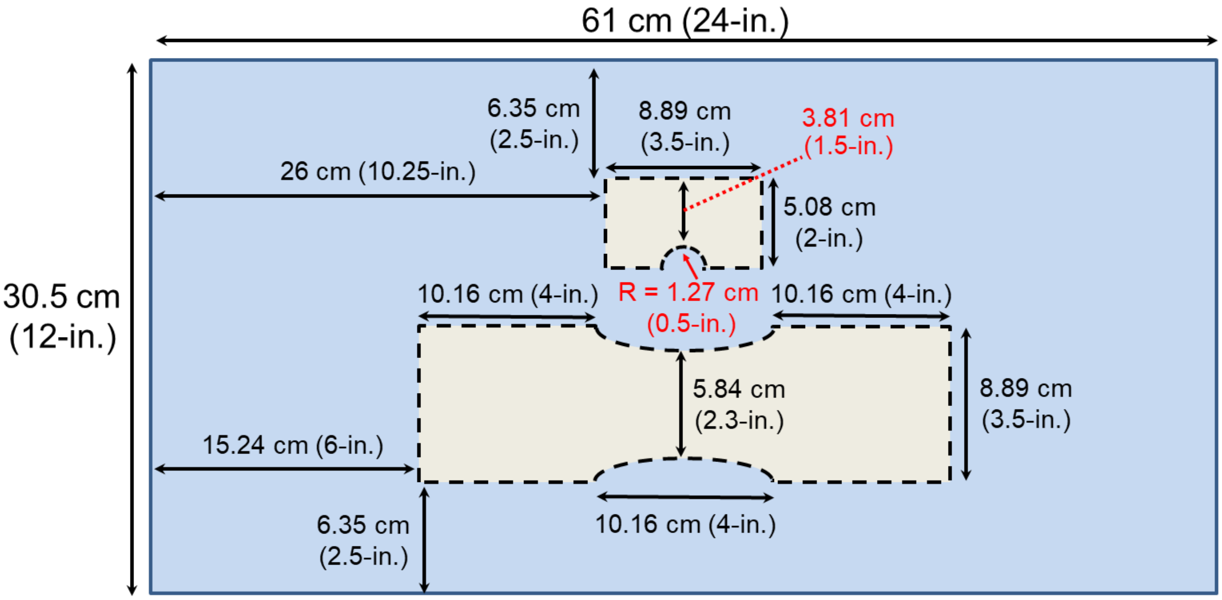

Figure A2. Schematic of the cutting diagram for the 25.4 mm (1-in.) thick HSLA-100 steel sub-plates showing the location of the dog-bone and reinforcement arch removed by water-jet cutting to serve as the basis for the final two "sister samples" for the project.

APPENDIX B: Supplementary Welded Fabrication Information

Table B1. Welding Parameters for Specimen #3

Pass	Bead	Avg. Voltage	Avg. Amperage	Travel Speed		Heat Input		Pre-Heat / Interpass	
				mm/s	ipm	J/mm	kJ/in	°C	°F
1	1	8.1	30.0	2.07	4.9	117	2.97	110	230
1	2	8.9	26.0	1.95	4.6	119	3.01	93.3	200
1	3	8.2	35.0	2.41	5.7	119	3.02	104.4	220
1	4	8.4	40.0	2.87	6.7	117	3.01	98.9	210
1	5	8.2	42.0	3.64	8.6	94.6	2.40	96.1	205
1	6	7.7	42.0	3.43	8.1	94.3	2.40	95.6	204
2	7	25.0	177.2	4.56	10.76	972	24.7	98.9	210
2	8	25.1	185.4	4.53	10.52	1043	26.5	112.8	235
2	9	24.7	178.0	3.76	8.89	1173	29.8	110	230
2	10	25.8	176.4	3.91	9.23	1165	29.6	101.7	215
2	11	25.8	182.3	4.42	10.43	1051	26.7	98.9	210
2	12	25.3	189.9	3.81	9.0	1260	32	94.4	202
3	13	25.3	189.6	4.22	9.97	1138	28.9	137.8	280
3	14	25.1	187.2	4.52	10.67	1039	26.4	106.7	224
3	15	25.3	187.8	4.72	11.14	1008	25.6	122.2	252
3	16	25.3	193.0	4.38	10.34	1114	28.3	115.6	240
4	17	25	182.2	4.69	11.08	972	24.7	95	203
4	18	24.9	184.4	4.25	10.04	1079	27.4	125.6	258
4	19	24.8	183.3	4.22	9.96	1079	27.4	113.9	237
4	20	25.3	186.3	4.69	11.08	1004	25.5	95	203

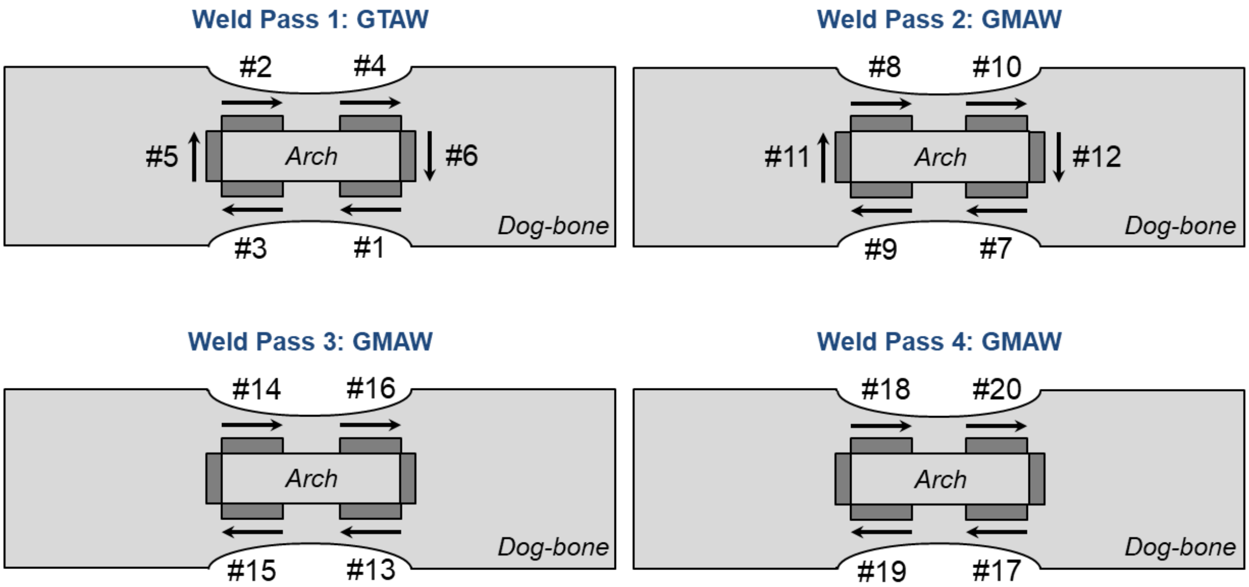

Figure B1. Schematic of the welding direction and sequence for each welding pass, including the initial GTAW beads (6), the first cover GMAW beads (6), the second cover GMAW beads (4), and the third cover GMAW beads (4).

This page intentionally left blank

DISTRIBUTION

EXTERNAL

Copies

DEFENSE TECHNICAL
INFORMATION CENTER 1
727 JOHN J KINGMAN ROAD
SUITE 0944
FORT BELVOIR, VA 22060-6218

ATTN: SEA 05P2
NAVAL SEA SYSTEMS COMMAND 4
1333 ISAAC HULL AVENUE S.E.
WASHINGTON NAVY YARD
WASHINGTON, DC 20376
ATTN: Archer, Bjornson, McGrorey, Melvin

ATTN: SEA 05P4
NAVAL SEA SYSTEMS COMMAND 1
1333 ISAAC HULL AVENUE S.E.
WASHINGTON NAVY YARD
WASHINGTON, DC 20376
ATTN: Rodgers

OFFICE OF NAVAL RESEARCH 3
875 N RANDOLPH ST
ARLINGTON, VA 22217
ATTN: Christodoulou, Hess, Mullins

CORNELL HIGH ENERGY SYNCHROTRON
SOURCE (CHESS) 5
161 SYNCHROTRON DRIVE
ITHACA, NY 14853
ATTN: Beaudoin, Budrow, Miller, Nygren, Woll

AIR FORCE RESEARCH LABORATORY 1
5135 PEARSON ROAD
WRIGHT-PATTERSON AFB, OH 45433
ATTN: Shade

NATIONAL INSTITUTE OF STANDARDS AND
TECHNOLOGY (NIST) 1
100 BUREAU DRIVE
GAITHERSBURG, MD 20899
ATTN: Gnaupel-Herold

OAK RIDGE NATIONAL INSTITUTE 1
1 BETHEL VALLEY RD
OAK RIDGE, TN 37830
ATTN: Bunn

NSWCCD INTERNAL DISTRIBUTION

Code	*Name*	*Copies*
60		1
60	Mercier	1
60	Rivera	1
604	Waters	1
61	DeLoach	1
611	Davis	1
611	Sinfield	1
611	Farren	1
611	Fisher	2
611	Bechetti	1
611	Semple	1
00T	Drazen	1
00T	Michalis	1
804	Stergiou	1
612	(Report Documentation Page)	1
613	(Report Documentation Page)	1
615	(Report Documentation Page)	1
617	(Report Documentation Page)	1
618	(Report Documentation Page)	1
619	(Report Documentation Page)	1
63	(Report Documentation Page)	1
65	(Report Documentation Page)	1
66	(Report Documentation Page)	1
3442	(TIC)	1

NAVSEA
WARFARE CENTERS
Carderock